

# Tensor Factorization via Transformed Tensor-Tensor Product for Image Alignment

Sijia Xia, Duo Qiu, and Xiongjun Zhang

**Abstract**—In this paper, we study the problem of a batch of linearly correlated image alignment, where the observed images are deformed by some unknown domain transformations, and corrupted by additive Gaussian noise and sparse noise simultaneously. By stacking these images as the frontal slices of a third-order tensor, we propose to utilize the tensor factorization method via transformed tensor-tensor product to explore the low-rankness of the underlying tensor, which is factorized into the product of two smaller tensors via transformed tensor-tensor product under any unitary transformation. The main advantage of transformed tensor-tensor product is that its computational complexity is lower compared with the existing literature based on transformed tensor nuclear norm. Moreover, the tensor  $\ell_p$  ( $0 < p < 1$ ) norm is employed to characterize the sparsity of sparse noise and the tensor Frobenius norm is adopted to model additive Gaussian noise. A generalized Gauss-Newton algorithm is designed to solve the resulting model by linearizing the domain transformations and a proximal Gauss-Seidel algorithm is developed to solve the corresponding subproblem. Furthermore, the convergence of the proximal Gauss-Seidel algorithm is established, whose convergence rate is also analyzed based on the Kurdyka-Łojasiewicz property. Extensive numerical experiments on real-world image datasets are carried out to demonstrate the superior performance of the proposed method as compared to several state-of-the-art methods in both accuracy and computational time.

**Index Terms**—Image alignment, transformed tensor-tensor product, tensor factorization, proximal Gauss-Seidel algorithm.

## I. INTRODUCTION

IMAGES and videos sharing in social networks have increased dramatically in the past decades. However, these images may suffer from various degradations during the acquirement and transmission process, such as impulse noise, partial occlusion, illumination variations, and misalignment [1], [2]. It is a vital task to recover these images from the observations with these degradations for subsequent applications including face recognition, image classification, and object tracking [3], [4]. In this paper, we study the problem of aligning a batch of linearly correlated images, which are deformed by some unknown domain transformations and corrupted by

The research of D. Qiu was supported in part by the National Natural Science Foundation of China under Grant No. 12201473 and the Science Foundation of Wuhan Institute of Technology under Grant No. K202256. The research of X. Zhang was supported in part by the National Natural Science Foundation of China under Grant No. 12171189 and the Knowledge Innovation Project of Wuhan under Grant No. 2022010801020279.

S. Xia is with the School of Mathematics and Statistics, Central China Normal University, Wuhan 430079, China (e-mail: sijiax@mails.ccnu.edu.cn).

D. Qiu is with the School of Mathematics and Physics, Wuhan Institute of Technology, Wuhan 430205, China (e-mail: quiduo13@wit.edu.cn).

X. Zhang is with the School of Mathematics and Statistics, and Hubei Key Laboratory of Mathematical Sciences, Central China Normal University, Wuhan 430079, China (e-mail: xjzhang@mail.ccnu.edu.cn).

sparse noise (such as impulse noise, partial occlusion) and Gaussian noise.

A lot of work has been done for the task of batch image alignment in the literature, where the images of an object or objects of interest are aligned to a fixed canonical template [5]. For example, Learned-Miller [6] present a congealing approach for a batch of image alignment, which aimed to minimize the sum of the pixel-stack entropies via transforming a set of images of a class. Here the main idea is to make a set of images appear as similar as possible by removing nuisance variables within these images. Cox et al. [7], [8] proposed least squares congealing methods for large number of image alignment by minimizing the sum of squared distances between pairs of images to acquire a low-rank matrix. Moreover, Vedaldi et al. [9] proposed to minimize a logarithmic determinant loss function to align a large collection of image data, which can be regarded as a smooth surrogate of the rank function. However, the above approaches may fail to align a batch of linearly correlated images effectively when there are large illumination variations and gross pixel corruptions or partial occlusion simultaneously, which often occurs in real-world images [2].

By unfolding the well-aligned and linearly correlated images into vectors and stacking these vectors as columns of a matrix, the resulting matrix is low-rank and some low-rank matrices based methods were proposed and studied for batch image alignment. For instance, Peng et al. [2] first proposed a robust image alignment method via seeking an optimal set of image domain transformations such that the matrix of the transformed images can be decomposed into the sum of a sparse error matrix and a low-rank matrix of the well-aligned images, where the misalignment of images was modeled as a domain transformation [10]. Then a sequence of convex programs that minimized the sum of  $\ell_1$  norm and nuclear norm of the two component matrices were proposed to approximate the previous problem by linearizing the domain transformations. Furthermore, in order to improve the computational efficiency, He et al. [11] proposed a low-rank matrix factorization method by minimizing the  $\ell_1$  norm of the error term and decomposing the underlying matrix into the product of two small matrices, where the first factor matrix belongs to an orthogonal subspace. However, the  $\ell_1$  norm is just suboptimal to obtain a sparse solution in statistic learning [12], [13], and some nonconvex penalized methods were proposed to improve the sparsity for variable selection [12], [14]. Moreover, Chen et al. [15] proposed a nonconvex model for noisy image alignment, where the nonconvex functions were employed onto the singular values of the well-aligned images

and each entry of the sparse error component, respectively. However, the matrix based methods will destroy the internal structure of these images by the unfolding approach. Besides, only the correlation of different images is utilized in these methods.

On the other hand, Wu et al. [5] proposed an online robust alignment method by using a low-rank matrix decomposition technique and then updating the basis online, where one needs to align a newly arrived image to previously well-aligned images. Then Song et al. [16] proposed to combine the geometric transformation with online principal component analysis to update the basis matrix online via a stochastic gradient descent algorithm for image alignment. Furthermore, Zheng et al. [17] proposed an online subspace learning approach from image gradient orientations for robust image alignment, which provides a more reliable low-dimensional subspace than that from pixel intensities. However, the online based methods need some well-aligned images in advance for seeking the basis matrix, which may be challenged when only noisy and misalignment images are available.

In order to explore the internal structure of these well-aligned images better, some tensor based methods were proposed and studied for image alignment, where each image is regarded as the frontal slice of a tensor. By using the domain transformed images to be decomposed into the sum of a low Tucker rank tensor and a sparse error tensor, Zhang et al. [18] proposed to employ the sum of nuclear norms of unfolding matrices of a tensor [19] to approximate the sum of entries of the Tucker rank of the underlying images, where the tensor  $\ell_1$  norm is used to characterize the sparsity of the error tensor. Li et al. [20] present an online robust low-rank tensor method by applying the matrix factorization technique for the unfolding matrices of a tensor to approximate its Tucker rank and the tensor  $\ell_1$  norm to approximate the sparse error. However, the tensor  $\ell_1$  norm may get a biased estimator for a sparse solution, which was demonstrated in statistical learning [12], [13]. Note that the sum of nuclear norms of unfolding matrices of a tensor utilizes the matrix nuclear norm to approximate the rank of the correspondingly unfolding matrix. While the nuclear norm of a matrix is just the  $\ell_1$  norm of the singular value vector, which also obtains a bias estimator [21]. Furthermore, Zhang et al. [22] extended the model in [18] to the nonconvex model by using  $\ell_p$  norm ( $0 < p < 1$ ) for each entry of the sparse error term and the singular values of the unfolding matrices of the underlying tensor for the low Tucker rank component. However, the sum of nuclear norms of unfolding matrices of a tensor is not the convex envelope of the sum of entries of the Tucker rank of a tensor [23], which is just suboptimal for tensor completion [24].

Recently, the tensor-tensor product and tensor singular value decomposition (SVD) based on tensor algebra operations were proposed for third-order tensors [25], [26], where the tensor-tensor product was the multiplication of a block-circulant matrix and a block column vector. Then Semerci et al. [27] proposed a tensor nuclear norm (TNN) method to approximate the multi-rank of a tensor for multienergy computed tomography. Moreover, Zhang et al. [28] applied the TNN for low-rank tensor completion in visual data based on tensor SVD,

and showed that the TNN is the tightest convex relaxation of the sum of multi-rank of a tensor. The TNN and tensor-tensor product are widely used in low-rank tensor recovery problems due to its superiority of characterising the low-rankness of a tensor, see [29]–[36] and references therein. However, the TNN is just the sum of nuclear norms of all frontal slice matrices of a tensor in the Fourier domain. And a limitation by using discrete Fourier transform is that the periodicity is assumed. Moreover, the discrete Fourier transform may not result in a low-rank tensor, while a low-rank requirement is preferred for low-rank tensor recovery [37]. In order to overcome the limitation of the Fourier transform in TNN, Song et al. [38] proposed a transformed tensor-tensor product and transformed tensor SVD under any unitary transformation for robust tensor completion, which can obtain a lower transformed multi-rank tensor by using suitable unitary transformations. The transformed tensor SVD based methods have been applied in various low-rank tensor optimization problems, see [37], [39]–[41] and references therein. While the above methods cannot be applied to the images with misalignment. Very recently, Qiu et al. [42] proposed a transformed tensor nuclear norm plus tensor  $\ell_1$  norm method for batch image alignment, where the images after domain transformations can be decomposed into the sum of a low transformed multi-rank tensor and a sparse error tensor. Moreover, they extended it to a family of nonconvex models based on transformed tensor nuclear norm, where the nonconvex functions are employed onto the singular values of all frontal slices of the underlying tensor in the transformed domain and each entry of the error tensor. However, the above method is very expensive in the computational complexity since one needs to compute the SVDs of all frontal slices of a tensor in the transformed domain.

In this paper, we propose a tensor factorization method for a batch of linearly correlated image alignment, where the observed images are deformed by some unknown domain transformations and corrupted by sparse noise (such as impulse noise, partial occlusion) and Gaussian noise simultaneously. By stacking these images into a third-order tensor along the third-dimension, the underlying tensor is factorized into the transformed tensor-tensor product of two smaller tensors under any unitary transformation, which is capable of reducing the computational complexity compared with the transformed tensor nuclear norm. Moreover, the tensor  $\ell_p$  norm ( $0 < p < 1$ ) is employed to enhance the sparsity of the sparse noise, where a sparser solution can be obtained than that of the tensor  $\ell_1$  norm. And the tensor Frobenius norm of the difference between the observation images with domain transformations and the underlying tensor, the sparse tensor, is utilized to characterize the Gaussian noise. Besides, a generalized Gauss-Newton algorithm [43] is developed to solve the proposed model by linearizing the domain transformations, where a proximal Gauss-Seidel algorithm is applied to solve the corresponding subproblem. Furthermore, the convergence of the proximal Gauss-Seidel algorithm is established under very mild conditions, whose convergence rate is also analyzed based on the Kurdyka-Łojasiewicz property [44]. Numerical examples on many real-world image datasets are reported to

demonstrate that the proposed approach outperforms many state-of-the-art ones in terms of visual quality and computational time for the task of image recovery and alignment.

The remaining parts of this paper are organized as follows. Section II is devoted to some notation and preliminaries about transformed tensor-tensor product under any unitary transformation for third-order tensors. In Section III, we propose a tensor factorization method based on transformed tensor-tensor product for image alignment. In Section IV, a generalized Gauss-Newton algorithm is designed to solve the resulting model and a proximal Gauss-Seidel algorithm is developed to solve the corresponding subproblem, where the convergence and convergent rate of this algorithm are established. Numerical examples are reported to demonstrate the effectiveness and efficiency of the proposed method in Section V. We conclude this paper in Section VI. The proofs of theorems are left in Appendix.

## II. PRELIMINARY

In this section, we give some notation of tensors and briefly introduce the definition of transformed tensor-tensor product under any unitary transformation.

### A. Notation and Notions

Scalars, vectors, matrices, and tensors are denoted by lowercase letters, lowercase boldface letters, uppercase boldface letters, and capital Euler script letters, respectively, e.g.,  $x, \mathbf{x}, \mathbf{X}, \mathcal{X}$ . The order of a tensor is the number of ways or modes [45]. For an arbitrary third-order tensor  $\mathcal{A} \in \mathbb{C}^{n_1 \times n_2 \times n_3}$ , its  $(i, j, k)$ th element is represented as  $\mathcal{A}_{ijk}$ . The  $i$ th frontal slice of  $\mathcal{A}$  is denoted as  $\mathbf{A}^{(i)} = \mathcal{A}(:, :, i)$ ,  $i = 1, 2, \dots, n_3$ . The  $(i, j)$ th tube of  $\mathcal{A}$  is denoted by  $\mathcal{A}(i, j, :)$ ,  $i = 1, \dots, n_1, j = 1, \dots, n_2$ .  $\mathcal{A}_{(3)}$  denotes the mode-3 unfolding of  $\mathcal{A}$ , which arranges the mode-3 fibers to be the columns of the resulting matrix. Here a fiber is defined by fixing every index but one [45]. Conversely, the inverse operator of mode-3 unfolding is denoted by  $\text{Fold}_3(\cdot)$ , i.e.,  $\text{Fold}_3(\mathcal{A}_{(3)}) = \mathcal{A}$ .

The inner product of two tensors  $\mathcal{A}, \mathcal{B} \in \mathbb{C}^{n_1 \times n_2 \times n_3}$  is defined as  $\langle \mathcal{A}, \mathcal{B} \rangle = \sum_{i=1}^{n_3} \text{Tr}(\mathbf{A}^{(i)}(\mathbf{B}^{(i)})^T)$ , where  $\text{Tr}(\cdot)$  denotes the trace of a matrix and  $\cdot^T$  denotes the conjugate transpose of a matrix. The tensor Frobenius norm of  $\mathcal{A}$  is defined as  $\|\mathcal{A}\|_F = \sqrt{\langle \mathcal{A}, \mathcal{A} \rangle}$ . The tensor  $\ell_p$  ( $0 < p < 1$ ) norm of  $\mathcal{A}$  is defined as  $\|\mathcal{A}\|_p = (\sum_{i,j,k} |\mathcal{A}_{ijk}|^p)^{\frac{1}{p}}$ .

For an extended real valued function  $f : \mathbb{R}^n \rightarrow [-\infty, +\infty]$ , its effective domain is defined as  $\text{dom}(f) = \{x \in \mathbb{R}^n : f(x) < +\infty\}$ . For a nonempty closed set  $K \subseteq \mathbb{R}^n$ , we use  $\text{dist}(\mathbf{x}, K)$  to denote the distance from  $\mathbf{x}$  to  $K$ , where  $\text{dist}(\mathbf{x}, K) = \inf_{\mathbf{z} \in K} \|\mathbf{x} - \mathbf{z}\|$ .

### B. Transformed Tensor-Tensor Product

In this subsection, we introduce the definition of the transformed tensor-tensor product under any unitary transformation for third-order tensors, which is adopted from [38], [46] directly. We denote a unitary matrix by  $\mathbf{U} \in \mathbb{C}^{n_3 \times n_3}$  satisfying  $\mathbf{U}\mathbf{U}^T = \mathbf{U}^T\mathbf{U} = \mathbf{I}_{n_3}$ , where  $\mathbf{I}_{n_3}$  is an  $n_3 \times n_3$  identity matrix.

For an arbitrary third-order tensor  $\mathcal{A} \in \mathbb{C}^{n_1 \times n_2 \times n_3}$ , we denote  $\hat{\mathcal{A}}_{\mathbf{U}}$  as the result of multiplying by  $\mathbf{U}$  on all tubes along the third-dimension of  $\mathcal{A}$ , i.e.,  $\hat{\mathcal{A}}_{\mathbf{U}}(i, j, :) = \mathbf{U}(\mathcal{A}(i, j, :))$ ,  $i = 1, \dots, n_1, j = 1, \dots, n_2$ . For simplicity, it is also expressed as  $\hat{\mathcal{A}}_{\mathbf{U}} = \mathbf{U}[\mathcal{A}]$ . Next, we define the block diagonal matrix  $\bar{\mathcal{A}}_{\mathbf{U}}$  as

$$\bar{\mathcal{A}}_{\mathbf{U}} = \text{bdiag}(\hat{\mathcal{A}}_{\mathbf{U}}) := \begin{bmatrix} \hat{\mathcal{A}}_{\mathbf{U}}^{(1)} & & \\ & \ddots & \\ & & \hat{\mathcal{A}}_{\mathbf{U}}^{(n_3)} \end{bmatrix},$$

where  $\hat{\mathcal{A}}_{\mathbf{U}}^{(k)}$  is the  $k$ th frontal slice of the tensor  $\hat{\mathcal{A}}_{\mathbf{U}}$ ,  $k = 1, \dots, n_3$ . The inverse operator of  $\text{bdiag}(\cdot)$ , denoted by  $\text{fold}_3(\cdot)$ , transforms the block diagonal matrix into a third-order tensor, where the  $i$ th frontal slice of the resulting tensor is the  $i$ th diagonal block, i.e.,  $\text{fold}_3(\text{bdiag}(\hat{\mathcal{A}}_{\mathbf{U}})) := \hat{\mathcal{A}}_{\mathbf{U}}$ .

Now we define the transformed tensor-tensor product via an arbitrary unitary matrix (called  $\mathbf{U}$ -product).

*Definition 1:* [38, Definition 1] The  $\mathbf{U}$ -product of arbitrary two tensors  $\mathcal{A} \in \mathbb{C}^{n_1 \times n_2 \times n_3}$ ,  $\mathcal{B} \in \mathbb{C}^{n_2 \times l \times n_3}$  is given by  $\mathcal{C} = \mathcal{A} \diamond_{\mathbf{U}} \mathcal{B} = \mathbf{U}^T[\text{fold}_3(\text{bdiag}(\hat{\mathcal{A}}_{\mathbf{U}}) \cdot \text{bdiag}(\hat{\mathcal{B}}_{\mathbf{U}}))]$ .

Note that  $\mathcal{C} = \mathcal{A} \diamond_{\mathbf{U}} \mathcal{B} \in \mathbb{C}^{n_1 \times l \times n_3}$  is equivalent to  $\bar{\mathcal{C}}_{\mathbf{U}} = \bar{\mathcal{A}}_{\mathbf{U}} \bar{\mathcal{B}}_{\mathbf{U}}$ , which can be shown as follows: First, by the definition of  $\mathbf{U}$ -product, we have

$$\begin{aligned} \mathcal{C} = \mathcal{A} \diamond_{\mathbf{U}} \mathcal{B} &= \mathbf{U}^T[\text{fold}_3(\text{bdiag}(\hat{\mathcal{A}}_{\mathbf{U}}) \cdot \text{bdiag}(\hat{\mathcal{B}}_{\mathbf{U}}))] \\ &= \mathbf{U}^T[\text{fold}_3(\bar{\mathcal{A}}_{\mathbf{U}} \cdot \bar{\mathcal{B}}_{\mathbf{U}})]. \end{aligned}$$

Moreover,

$$\begin{aligned} \bar{\mathcal{C}}_{\mathbf{U}} &= \text{bdiag}(\hat{\mathcal{C}}_{\mathbf{U}}) = \text{bdiag}(\mathbf{U}[\mathcal{C}]) \\ &= \text{bdiag}(\mathbf{U}[\mathbf{U}^T[\text{fold}_3(\bar{\mathcal{A}}_{\mathbf{U}} \cdot \bar{\mathcal{B}}_{\mathbf{U}})]]) \\ &= \text{bdiag}([\text{fold}_3(\bar{\mathcal{A}}_{\mathbf{U}} \cdot \bar{\mathcal{B}}_{\mathbf{U}})]) = \bar{\mathcal{A}}_{\mathbf{U}} \bar{\mathcal{B}}_{\mathbf{U}}. \end{aligned}$$

*Definition 2:* [38, Definition 2] The conjugate transpose of a tensor  $\mathcal{A} \in \mathbb{C}^{n_1 \times n_2 \times n_3}$  with respect to any unitary matrix  $\mathbf{U} \in \mathbb{C}^{n_3 \times n_3}$  is a tensor  $\mathcal{A}^T \in \mathbb{C}^{n_2 \times n_1 \times n_3}$  given by  $\mathcal{A}^T = \mathbf{U}^T[\text{fold}_3(\text{bdiag}(\hat{\mathcal{A}}_{\mathbf{U}})^T)]$ .

*Definition 3:* [46, Proposition 4.1] Let each frontal slice of  $\mathcal{T} \in \mathbb{R}^{n \times n \times n}$  be the  $n \times n$  identity matrix. The identity tensor  $\mathcal{I} \in \mathbb{C}^{n \times n \times n}$  with respect to  $\mathbf{U}$  is defined as  $\mathcal{I} = \mathbf{U}^T[\mathcal{T}]$ .

*Definition 4:* [46, Definition 4.3] The inverse of a tensor  $\mathcal{A} \in \mathbb{C}^{n \times n \times n}$  with respect to  $\mathbf{U}$ , denoted by  $\mathcal{A}^{-1}$ , is defined as  $\mathcal{A}^{-1} \diamond_{\mathbf{U}} \mathcal{A} = \mathcal{A} \diamond_{\mathbf{U}} \mathcal{A}^{-1} = \mathcal{I}$ .

*Definition 5:* [46, Definition 5.1] If a tensor  $\mathcal{P} \in \mathbb{C}^{n \times n \times n}$  with respect to  $\mathbf{U}$ -product satisfies  $\mathcal{P}^T \diamond_{\mathbf{U}} \mathcal{P} = \mathcal{P} \diamond_{\mathbf{U}} \mathcal{P}^T = \mathcal{I}$ , then  $\mathcal{P}$  is a unitary tensor.

A diagonal tensor is defined that each frontal slice of the tensor is a diagonal matrix [25]. Now we give the definition of the transformed tensor SVD of a third-order tensor.

*Definition 6:* [46, Theorem 5.1] The transformed tensor SVD of  $\mathcal{A} \in \mathbb{C}^{n_1 \times n_2 \times n_3}$  is defined as  $\mathcal{A} = \mathcal{U} \diamond_{\mathbf{U}} \Sigma \diamond_{\mathbf{U}} \mathcal{V}^T$ , where  $\Sigma \in \mathbb{C}^{n_1 \times n_2 \times n_3}$  is a diagonal tensor,  $\mathcal{U} \in \mathbb{C}^{n_1 \times n_1 \times n_3}$ ,  $\mathcal{V} \in \mathbb{C}^{n_2 \times n_2 \times n_3}$  are unitary tensors with respect to  $\mathbf{U}$ -product.

*Definition 7:* [38, Definition 6] For an arbitrary tensor  $\mathcal{A} \in \mathbb{C}^{n_1 \times n_2 \times n_3}$ , its transformed multi-rank is a vector  $\mathbf{r} = (r_1, r_2, \dots, r_{n_3}) \in \mathbb{R}^{n_3}$  with  $r_i = \text{rank}(\hat{\mathcal{A}}_{\mathbf{U}}^{(i)})$ ,  $i = 1, 2, \dots, n_3$ . Let  $\mathcal{A} = \mathcal{U} \diamond_{\mathbf{U}} \Sigma \diamond_{\mathbf{U}} \mathcal{V}^T$ . The transformed tubal

rank  $\hat{r}$  of  $\mathcal{A}$  is defined as the number of nonzero tubes of  $\Sigma$ , i.e.,  $\hat{r} = \#\{i : \Sigma(i, i, :) \neq 0\} = \max\{r_1, r_2, \dots, r_{n_3}\}$ , where  $\#\{\cdot\}$  denotes the cardinality of a set.

### III. TRANSFORMED TENSOR-TENSOR PRODUCT FOR IMAGE ALIGNMENT

In this section, we first formulate the problem of batch image alignment based on the tensor structure, and then propose a tensor factorization model via transformed tensor-tensor product under any unitary transformation for a batch of linearly correlated image alignment, where the observed images are deformed by some unknown domain transformations and corrupted by additive Gaussian noise and sparse noise simultaneously.

#### A. Problem Formulation

Given  $n_3$  well-aligned images  $\mathbf{L}_i \in \mathbb{R}^{n_1 \times n_2}$  of the same object,  $i = 1, 2, \dots, n_3$ . These images  $\mathbf{L}_i$  are stacked into a third-order tensor  $\mathcal{L} \in \mathbb{R}^{n_1 \times n_2 \times n_3}$ , whose  $i$ th frontal slice is the image  $\mathbf{L}_i$ . As a result, the tensor data  $\mathcal{L}$  generated by the linearly correlated image has a low rank structure. However, these images with same objects or scenes may not be well-aligned, which can be modeled as domain deformations, such as affine transformation, similarity transformation, translation transformation [10]. Assume that the domain transformations  $\tau_i \in \mathbb{R}^m$  are from a finite-dimensional group  $\mathbb{G}$ . Then we apply the transformation  $\tau_i$  to each image given by

$$(\mathcal{D} \circ \tau)(:, :, i) = \mathcal{D}(:, :, i) \circ \tau_i,$$

where  $\tau = \{\tau_1, \tau_2, \dots, \tau_{n_3}\}$  is the domain transformation,  $\mathcal{D}$  denotes the misaligned images, and  $\mathcal{D} \circ \tau \in \mathbb{R}^{n_1 \times n_2 \times n_3}$  represents the well-aligned images via the domain transformation  $\tau$  [2], [22]. However, in real-world applications, the observed images not only suffer from misalignment, but also are corrupted by additive Gaussian noise and sparse noise simultaneously. Mathematically, the observed model can be described as

$$\mathcal{D} \circ \tau = \mathcal{L} + \mathcal{S} + \mathcal{N}, \quad (1)$$

where  $\tau$  represents the domain transformation,  $\mathcal{L}$  denotes the clear and well-aligned images,  $\mathcal{S}$  and  $\mathcal{N}$  denote the sparse noise and Gaussian noise, respectively. Then we aim to recover  $\mathcal{L}$  from the noisy and misaligned observations  $\mathcal{D}$ .

#### B. Tensor Factorization Model via Transformed Tensor-Tensor Product

In this subsection, we propose a tensor factorization method based on U-product for aligning a batch of linearly correlated images, which can handle large-scale image data effectively.

For the underlying tensor  $\mathcal{L}$  in (1), we propose to utilize the transformed tensor-tensor product to explore its global low-rankness, where the underlying tensor can be decomposed into the U-product of two small tensors under any unitary transformation. In this situation, the transformed tubal rank of the underlying tensor is low. More precisely, assume that the transformed tubal rank of  $\mathcal{L} \in \mathbb{R}^{n_1 \times n_2 \times n_3}$  is  $r$ . Then  $\mathcal{L}$  is factorized into the U-product of two small tensors

$\mathcal{X} \in \mathbb{R}^{n_1 \times r \times n_3}$  and  $\mathcal{Y} \in \mathbb{R}^{r \times n_2 \times n_3}$  such that  $\mathcal{L} = \mathcal{X} \diamond_{\mathbf{U}} \mathcal{Y}$ . In this case, if  $r$  is small, the transformed tubal rank of  $\mathcal{L}$  is low. Then the computational complexity of U-product is much lower than that of the transformed tensor nuclear norm method in [42]. Moreover, the tensor  $\ell_p$  norm is utilized to characterise the sparseness of the sparse noise, where  $0 < p < 1$ . Compared with the tensor  $\ell_1$  norm, the tensor  $\ell_p$  norm can obtain a sparser solution [47]. For Gaussian noise, we use the tensor Frobenius norm of the difference among  $\mathcal{D} \circ \tau$ , the underlying tensor with U-product, and sparse noise. Therefore, we propose the following model for a batch of image alignment:

$$\min_{\tau, \mathcal{X}, \mathcal{Y}, \mathcal{S}} \frac{1}{2} \|\mathcal{D} \circ \tau - \mathcal{X} \diamond_{\mathbf{U}} \mathcal{Y} - \mathcal{S}\|_F^2 + \lambda \|\mathcal{S}\|_p^p, \quad (2)$$

where  $\lambda > 0$  is a given constant.

*Remark 1:* In model (2), we propose to utilize the transformed tensor-tensor product via any unitary transformation to explore the low-rankness of these images, which can reduce the computational complexity compared with the transformed tensor nuclear norm method in [42] if the transformed tubal rank is small. And the superiority of the transformed tensor-tensor product is that the lower transformed multi-rank will be obtained under suitable unitary transformation compared with the tensor-tensor product based on Fourier transform in [25]. Moreover, the tensor  $\ell_p$  norm ( $0 < p < 1$ ) is used to enhance the sparsity of the error tensor, which can generate a sparser solution as compared to the tensor  $\ell_1$  norm. This is similar to the  $\ell_p$  optimization problem in compressed sensing and matrix completion [47].

*Remark 2:* For the matrix based methods in [2], [15] for image alignment, one needs to unfold the images into vectors and stack these vectors as columns of a matrix, which is low-rank since the linear correlation of the images. However, the unfolding method will destroy the internal structure of these images and only utilizes the correlation among different images. The tensor based method can explore the low-rankness better since both the correlation among these images and the correlation of each image are used.

*Remark 3:* Compared with the model in [22], which used  $\ell_p$  norm based the sum of nuclear norms of unfolding matrices of a tensor to approximate the sum of entries of its Tucker rank, we used the transformed tensor-tensor product to approximate the transformed tubal rank of a tensor. Moreover, the sum of nuclear norms of unfolding matrices of a tensor is not the tightest convex relaxation of the sum of entries of the Tucker rank of a tensor [23], which implies that the sum of nuclear norms of the unfolding matrices of a tensor is just suboptimal. Besides, the transformed tensor SVD based methods perform better than the Tucker rank based methods in low-rank tensor recovery, see [37], [39], [41], [42] and references therein.

*Remark 4:* Compared with the model in [42], which used the transformed tensor nuclear norm based method to characterise the low-rankness of the underlying tensor, we employ the U-product to enhance the low-rankness of the underlying tensor. The main superiority of U-product is that lower computational complexity is required, which avoids the SVD of the frontal slices of the underlying tensor in the transformed domain.

#### IV. OPTIMIZATION ALGORITHM

In this section, a generalized Gauss-Newton algorithm [43] is developed to solve the proposed model (2), where a proximal Gauss-Seidel algorithm [48] is designed to solve the resulting subproblem. Then, the convergence and convergence rate of the proximal Gauss-Seidel algorithm are established under very mild conditions.

##### A. Generalized Gauss-Newton Algorithm

By the nonlinearity of the formula  $\mathcal{D} \circ \tau$ , one cannot solve problem (2) directly. We develop a generalized Gauss-Newton algorithm to solve (2), which is based on a linear approximation to the nonlinear term in the objective. When the change in  $\tau$  is small, we linearize the formula  $\mathcal{D} \circ \tau$  by the first-order Taylor expansion. A similar technique has been widely used in the existing literature [2], [22], [42]. Suppose that the initial transformation  $\tau^t \in \mathbb{G}$  is known and  $\mathbb{G}$  is some  $m$ -parameter group. For  $\Delta\tau_i \in \mathbb{R}^m$  and  $\Delta\tau = [\Delta\tau_1, \Delta\tau_2, \dots, \Delta\tau_{n_3}] \in \mathbb{R}^{m \times n_3}$ , we have

$$\begin{aligned} \mathcal{D} \circ \tau &\approx \mathcal{D} \circ (\tau^t + \Delta\tau) \\ &\approx \mathcal{D} \circ \tau^t + \text{Fold}_3\left(\left(\sum_{i=1}^{n_3} \mathbf{J}_i \Delta\tau_i \varepsilon_i^T\right)^T\right), \end{aligned} \quad (3)$$

where  $\mathbf{J}_i$  represents the Jacobian of the  $i$ th image with respect to the domain transformation parameter  $\tau_i^t$ ,  $\varepsilon_i$  denotes the standard basis in  $\mathbb{R}^{n_3}$ ,  $i = 1, 2, \dots, n_3$ , and  $\text{Fold}_3(\cdot)$  is the inverse operator of mode-3 unfolding of a third-order tensor. In this case, problem (2) can be relaxed to the following nonconvex optimization problem:

$$\begin{aligned} \min_{\mathcal{X}, \mathcal{Y}, \mathcal{S}, \Delta\tau} \quad & \frac{1}{2} \|\mathcal{D} \circ \tau^t + \Delta\Gamma - \mathcal{X} \diamond_{\mathbf{U}} \mathcal{Y} - \mathcal{S}\|_F^2 + \lambda \|\mathcal{S}\|_p^p \\ & + \frac{\rho_1}{2} \|\mathcal{X}\|_F^2 + \frac{\rho_2}{2} \|\mathcal{Y}\|_F^2 + \frac{\rho_3}{2} \|\Delta\tau\|_F^2, \end{aligned} \quad (4)$$

where  $\rho_1, \rho_2, \rho_3 > 0$  are given constants and  $\Delta\Gamma = \text{Fold}_3((\sum_{i=1}^{n_3} \mathbf{J}_i \Delta\tau_i \varepsilon_i^T)^T)$ . Here we add a quadratic term  $\frac{\rho_3}{2} \|\Delta\tau\|_F^2$  to prevent  $\Delta\tau$  from being too large since the Taylor expansion of  $\tau$  is only locally valid. Moreover, the quadratic terms with respect to  $\mathcal{X}$  and  $\mathcal{Y}$  are used to guarantee the uniqueness of the corresponding solutions.

When one get the solution of  $\Delta\tau$  by solving model (4),  $\tau^t$  is updated by  $\tau^t + \Delta\tau$  in the next iteration, which is the main idea of the generalized Gauss-Newton algorithm [43] and has been widely applied in image alignment [2], [5], [22], [42]. The iterative process of the generalized Gauss-Newton algorithm is stated in Algorithm 1. Moreover, in order to eliminate trivial solutions, such as zooming in a single dark pixel or dark area in the image, we normalize the image data by  $\frac{\mathcal{D}(:, :, i) \circ \tau_i^t}{\|\mathcal{D}(:, :, i) \circ \tau_i^t\|_F}$  at the  $t$ th iteration.

##### B. Proximal Gauss-Seidel Algorithm

The key step of Algorithm 1 is to solve problem (4). Now we design a proximal Gauss-Seidel algorithm [48] to compute it. Let

$$\begin{aligned} F(\mathcal{X}, \mathcal{Y}, \mathcal{S}, \Delta\tau) &:= Q(\mathcal{X}, \mathcal{Y}, \mathcal{S}, \Delta\tau) + \lambda \|\mathcal{S}\|_p^p \\ &+ \frac{\rho_1}{2} \|\mathcal{X}\|_F^2 + \frac{\rho_2}{2} \|\mathcal{Y}\|_F^2 + \frac{\rho_3}{2} \|\Delta\tau\|_F^2, \end{aligned} \quad (5)$$

---

#### Algorithm 1 A Generalized Gauss-Newton Algorithm for Solving (2)

---

**Initialization:** Image data  $\mathcal{D} \in \mathbb{R}^{n_1 \times n_2 \times n_3}$ . Given  $\lambda > 0$  and an initial transformation  $\tau^0 \in \mathbb{G}$ . For  $t = 0, 1, 2, \dots$

**repeat**

**Step 1.** Calculate the Jacobian matrices:

$$\mathbf{J}_i = \frac{\partial}{\partial \tau_i^t} \left( \frac{\mathcal{D}(:, :, i) \circ \tau_i^t}{\|\mathcal{D}(:, :, i) \circ \tau_i^t\|_F} \right) \Big|_{\tau_i^t}, \quad i = 1, 2, \dots, n_3.$$

**Step 2.** Warp and normalize  $\mathcal{D} \circ \tau^t$ :

$$(\mathcal{D} \circ \tau^t)(:, :, i) = \frac{\mathcal{D}(:, :, i) \circ \tau_i^t}{\|\mathcal{D}(:, :, i) \circ \tau_i^t\|_F}.$$

**Step 3.** Compute  $(\mathcal{X}, \mathcal{Y}, \mathcal{S}, \Delta\tau)$  by solving (4).

**Step 4.** Update  $\tau^{t+1} = \tau^t + \Delta\tau$ .

**until** A stopping condition is satisfied.

---

where

$$Q(\mathcal{X}, \mathcal{Y}, \mathcal{S}, \Delta\tau) := \frac{1}{2} \|\mathcal{D} \circ \tau^t + \Delta\Gamma - \mathcal{X} \diamond_{\mathbf{U}} \mathcal{Y} - \mathcal{S}\|_F^2. \quad (6)$$

Then the iterations of the proximal Gauss-Seidel algorithm for solving (4) can be given explicitly as follows:

$$\mathcal{X}^{k+1} = \underset{\mathcal{X}}{\text{argmin}} F(\mathcal{X}, \mathcal{Y}^k, \mathcal{S}^k, \Delta\tau^k) + \frac{\alpha^k}{2} \|\mathcal{X} - \mathcal{X}^k\|_F^2, \quad (7)$$

$$\mathcal{Y}^{k+1} = \underset{\mathcal{Y}}{\text{argmin}} F(\mathcal{X}^{k+1}, \mathcal{Y}, \mathcal{S}^k, \Delta\tau^k) + \frac{\beta^k}{2} \|\mathcal{Y} - \mathcal{Y}^k\|_F^2, \quad (8)$$

$$\mathcal{S}^{k+1} = \underset{\mathcal{S}}{\text{argmin}} F(\mathcal{X}^{k+1}, \mathcal{Y}^{k+1}, \mathcal{S}, \Delta\tau^k) + \frac{\gamma^k}{2} \|\mathcal{S} - \mathcal{S}^k\|_F^2, \quad (9)$$

$$\Delta\tau^{k+1} = \underset{\Delta\tau}{\text{argmin}} F(\mathcal{X}^{k+1}, \mathcal{Y}^{k+1}, \mathcal{S}^{k+1}, \Delta\tau) + \frac{\xi^k}{2} \|\Delta\tau - \Delta\tau^k\|_F^2, \quad (10)$$

where  $\alpha^k, \beta^k, \gamma^k, \xi^k > 0$  are the given parameters. Now the explicit solutions of each subproblem in (7)-(10) are given below.

- Problem (7) can be reformulated equivalently as

$$\begin{aligned} \mathcal{X}^{k+1} &= \underset{\mathcal{X}}{\text{argmin}} \frac{1}{2} \|\mathcal{B}^k - \mathcal{X} \diamond_{\mathbf{U}} \mathcal{Y}^k\|_F^2 \\ &+ \frac{\rho_1 + \alpha^k}{2} \left\| \mathcal{X} - \frac{\alpha^k}{\rho_1 + \alpha^k} \mathcal{X}^k \right\|_F^2, \end{aligned} \quad (11)$$

where

$$\mathcal{B}^k = \mathcal{D} \circ \tau^t + \Delta\Gamma^k - \mathcal{S}^k. \quad (12)$$

with  $\Delta\Gamma^k = \text{Fold}_3((\sum_{i=1}^{n_3} \mathbf{J}_i \Delta\tau_i^k \varepsilon_i^T)^T)$ . Then the optimal solution  $\mathcal{X}^{k+1}$  of (11) is given by

$$\begin{aligned} \mathcal{X}^{k+1} &= (\mathcal{B}^k \diamond_{\mathbf{U}} (\mathcal{Y}^k)^T + \alpha^k \mathcal{X}^k) \diamond_{\mathbf{U}} (\mathcal{Y}^k \diamond_{\mathbf{U}} (\mathcal{Y}^k)^T \\ &+ (\rho_1 + \alpha^k) \mathcal{I})^{-1}, \end{aligned} \quad (13)$$

where  $\mathcal{I} \in \mathbb{C}^{r \times r \times n_3}$  denotes the identity tensor.

- Problem (8) can be rewritten as

$$\begin{aligned} \mathcal{Y}^{k+1} &= \underset{\mathcal{Y}}{\text{argmin}} \frac{1}{2} \|\mathcal{B}^k - \mathcal{X}^{k+1} \diamond_{\mathbf{U}} \mathcal{Y}\|_F^2 \\ &+ \frac{\rho_2 + \beta^k}{2} \left\| \mathcal{Y} - \frac{\beta^k}{\rho_2 + \beta^k} \mathcal{Y}^k \right\|_F^2, \end{aligned} \quad (14)$$

where  $\mathcal{B}^k$  is defined as (12). The optimal solution  $\mathcal{Y}^{k+1}$  of (14) takes the form of

$$\begin{aligned} \mathcal{Y}^{k+1} &= ((\mathcal{X}^{k+1})^T \diamond_{\mathbf{U}} \mathcal{X}^{k+1} + (\rho_2 + \beta^k) \mathcal{I})^{-1} \\ &\quad \diamond_{\mathbf{U}} ((\mathcal{X}^{k+1})^T \diamond_{\mathbf{U}} \mathcal{B}^k + \beta^k \mathcal{Y}^k). \end{aligned} \quad (15)$$

- Problem (9) is equivalent to

$$\mathcal{S}^{k+1} = \operatorname{argmin}_{\mathcal{S}} \lambda \|\mathcal{S}\|_p^p + \frac{1 + \gamma^k}{2} \|\mathcal{S} - \mathcal{H}^k\|_F^2, \quad (16)$$

where

$$\mathcal{H}^k = \frac{1}{1 + \gamma_k} (\mathcal{D} \circ \tau^t + \Delta \Gamma^k - \mathcal{X}^{k+1} \diamond_{\mathbf{U}} \mathcal{Y}^{k+1} + \gamma^k \mathcal{S}^k).$$

Note that problem (16) is just the thresholding of the  $\ell_p$  optimization problem ( $0 < p < 1$ ) for the tensor case. By [47, Theorem 1], one can deduce

$$(\mathcal{S}^{k+1})_{ijt} = \begin{cases} 0, & \text{if } |(\mathcal{H}^k)_{ijt}| < \mu^*, \\ \{0, \operatorname{sgn}((\mathcal{H}^k)_{ijt}) \bar{b}\}, & \text{if } |(\mathcal{H}^k)_{ijt}| = \mu^*, \\ \operatorname{sgn}((\mathcal{H}^k)_{ijt}) \bar{b}^*, & \text{if } |(\mathcal{H}^k)_{ijt}| > \mu^*, \end{cases} \quad (17)$$

where  $\operatorname{sgn}(\cdot)$  denotes the signum function,  $\bar{b} = (\frac{2\lambda(1-p)}{1+\gamma^k})^{\frac{1}{2-p}}$ ,  $\mu^* = \bar{b} + \frac{\lambda p \bar{b}^{p-1}}{1+\gamma^k}$ , and  $\bar{b}^*$  is the largest solution to the equation  $b + \frac{\lambda}{1+\gamma^k} p b^{p-1} = |(\mathcal{H}^k)_{ijt}|$  with  $b > 0$ , which can be obtained from the iteration

$$b^{s+1} = |(\mathcal{H}^k)_{ijt}| - \frac{\lambda}{1 + \gamma^k} p (b^s)^{p-1} \quad (18)$$

with the initial value  $b^0 \in (\bar{b}, |(\mathcal{H}^k)_{ijt}|)$ ,  $s = 0, 1, 2, \dots$

- Let  $\mathcal{C}^{k+1} = \mathcal{D} \circ \tau^t - \mathcal{X}^{k+1} \diamond_{\mathbf{U}} \mathcal{Y}^{k+1} - \mathcal{S}^{k+1}$ . Then problem (10) can be reformulated equivalently as

$$\begin{aligned} \Delta \tau^{k+1} &= \operatorname{argmin}_{\Delta \tau} \frac{\rho_3 + \xi^k}{2} \left\| \Delta \tau - \frac{\xi^k}{\rho_3 + \xi^k} \Delta \tau^k \right\|_F^2 \\ &\quad + \frac{1}{2} \left\| \operatorname{Fold}_3 \left( \left( \sum_{i=1}^{n_3} \mathbf{J}_i \Delta \tau \varepsilon_i \varepsilon_i^T \right)^T \right) + \mathcal{C}^{k+1} \right\|_F^2. \end{aligned}$$

It follows from [42, Theorem 3] that

$$\begin{aligned} \Delta \tau^{k+1} &= \sum_{i=1}^{n_3} \left( \mathbf{J}_i^T \mathbf{J}_i + (\rho_3 + \xi^k) \mathbf{I} \right)^{-1} \left( \xi^k \Delta \tau^k \right. \\ &\quad \left. - \mathbf{J}_i^T (\mathcal{C}^{k+1})^T \right) \varepsilon_i \varepsilon_i^T, \end{aligned} \quad (19)$$

where  $\mathbf{I}$  denote the  $m \times m$  identity matrix.

Now the proximal Gauss-Seidel algorithm for solving problem (4) is summarized in Algorithm 2.

**Remark 5:** The parameters  $\alpha^k, \beta^k, \gamma^k, \xi^k$  in Algorithm 2 are just needed to have lower and upper bounds in the implementation, which is used to guarantee the convergence of Algorithm 2.

**Remark 6:** The computational complexity of Algorithm 2 is given as follows. For any two tensors  $\mathcal{A} \in \mathbb{R}^{n_1 \times r \times n_3}, \mathcal{B} \in \mathbb{R}^{r \times n_2 \times n_3}$ , and unitary matrix  $\mathbf{U} \in \mathbb{C}^{n_3 \times n_3}$ , the complexity of performing a unitary matrix ( $n_3 \times n_3$ ) to an  $n_3$ -tube is  $O(n_3^2)$ . The complexity of performing the matrix-matrix product of the frontal slices is  $O(r n_1 n_2)$  after unitary transformations. Therefore, the computational complexity of  $\mathcal{A} \diamond_{\mathbf{U}} \mathcal{B}$  is  $O(r n_1 n_2 n_3 + \max\{n_1, n_2\} r n_3^2)$ . The computational complexity of the inverse of an  $n \times n \times n_3$  tensor is

$O(n^2 n_3^2 + n^3 n_3)$ . Assume that  $r \leq \min\{n_1, n_2\}$  and  $m \leq n_3$ . Then the computational complexity of computing  $\mathcal{X}^{k+1}$  is  $O(r n_1 n_2 n_3 + n_1 n_2 n_3^2)$ . Similarly, the computational complexity of computing  $\mathcal{Y}^{k+1}$  is  $O(r n_1 n_2 n_3 + n_1 n_2 n_3^2)$ . Moreover, the computational cost of  $\mathcal{S}^{k+1}$  is  $O(n_1 n_2 n_3 n_s)$ , where  $n_s$  is the maximum number of iterations for solving (18). And the computational cost of  $\Delta \tau^{k+1}$  is  $O(m n_1 n_2 n_3 + m n_3^2)$ . As a result, the computational complexity of the proximal Gauss-Seidel algorithm is  $O(r n_1 n_2 n_3 + n_1 n_2 n_3^2 + n_1 n_2 n_3 n_s + m n_3^2)$ .

**Algorithm 2** A Proximal Gauss-Seidel Algorithm for Solving Problem (4).

---

**Initialization:** Given  $\mathcal{X}^0, \mathcal{Y}^0, \mathcal{S}^0, \Delta \tau^0, \lambda, \rho_1, \rho_2, \rho_3 > 0, \underline{d} \leq \alpha^k, \beta^k, \gamma^k, \xi^k \leq \bar{d}, 0 < \underline{d} < \bar{d} < +\infty$ .

**repeat**

- Step 1.** Update  $\mathcal{X}^{k+1}$  by (13).
- Step 2.** Update  $\mathcal{Y}^{k+1}$  by (15).
- Step 3.** Update  $\mathcal{S}^{k+1}$  by (17).
- Step 4.** Update  $\Delta \tau^{k+1}$  by (19).

**until** A stopping condition is satisfied.

---

**Remark 7:** The main difference between [42] and our proposed algorithm in Algorithm 2 is the computations of  $\mathcal{X}^{k+1}, \mathcal{Y}^{k+1}$  and the transformed tensor nuclear norm. Assume that  $n_2 \leq n_1$ , then the computational complexity of the transformed tensor nuclear norm in [42] is  $O(n_1 n_2^2 n_3 + n_1 n_2 n_3^2)$ , while the computational cost of  $\mathcal{X}^{k+1}, \mathcal{Y}^{k+1}$  is  $O(r n_1 n_2 n_3 + n_1 n_2 n_3^2)$ . Therefore, if  $r$  is much smaller than  $n_2$ , the computational complexity of Algorithm 2 is much lower than that in [42]. Note that  $r$  is much smaller than  $\min\{n_1, n_2\}$  in general since a low-rank requirement is preferred for a batch of linearly correlated image alignment.

### C. Convergence Analysis

In this subsection, the convergence of the proximal Gauss-Seidel algorithm is established, which is stated in the following theorem.

**Theorem 1:** Supposed that  $0 < \underline{d} < \bar{d} < +\infty$  are given constants. Assume that  $\underline{d} \leq \alpha^k, \beta^k, \gamma^k, \xi^k \leq \bar{d}$  and  $p$  is rational. Let  $\{(\mathcal{X}^k, \mathcal{Y}^k, \mathcal{S}^k, \Delta \tau^k)\}$  be the sequence generated by Algorithm 2. Then the sequence  $\{(\mathcal{X}^k, \mathcal{Y}^k, \mathcal{S}^k, \Delta \tau^k)\}$  converges to a critical point of  $F(\mathcal{X}, \mathcal{Y}, \mathcal{S}, \Delta \tau)$  in (5).

**Remark 8:** The assumptions in Theorem 1 are very mild. One only needs  $p$  to be rational and  $\alpha^k, \beta^k, \gamma^k, \xi^k$  to be bounded from below and above for any  $k$ .

### D. Rate of Convergence

In this subsection, we establish the rate of convergence of the proximal Gauss-Seidel algorithm for solving problem (4). Before proceeding with the analysis, we introduce some properties of the sequence  $\{(\mathcal{X}^k, \mathcal{Y}^k, \mathcal{S}^k, \Delta \tau^k)\}$  generated by Algorithm 2. To simplify the notation for the following analysis, we denote  $\mathcal{Z}^k = (\mathcal{X}^k, \mathcal{Y}^k, \mathcal{S}^k, \Delta \tau^k)$ .

The KL exponent, which is defined in Appendix A, is closely related to the convergence rate of many descent algorithms [49], [50]. Note that the proper closed semi-algebraic functions are KL functions with exponent  $\theta \in [0, 1]$  (e.g.,

[50]–[52]), which implies that  $F(\mathcal{X}, \mathcal{Y}, \mathcal{S}, \Delta\tau)$  in (5) is a KL function with exponent  $\theta \in [0, 1]$ . In the following, we state the main result with respect to the convergence rate of the proximal Gauss-Seidel algorithm in Algorithm 2.

**Theorem 2:** Let  $\{\mathcal{Z}^k\}$  be a sequence generated by Algorithm 2, whose limit point is denoted by  $\mathcal{Z}^*$ , and  $\theta \in [0, 1]$  be the KL exponent of  $F$ . Suppose that  $p$  is rational. Then the following assertions hold:

(i) If  $\theta = 0$ , then the sequence  $\{\mathcal{Z}^k\}$  converges in a finite number of steps.

(ii) If  $\theta \in (0, \frac{1}{2}]$ , then the sequence  $\{\mathcal{Z}^k\}$  converges R-linearly, i.e., there exist  $c > 0$  and  $\vartheta \in (0, 1)$  such that  $\|\mathcal{Z}^k - \mathcal{Z}^*\|_F \leq c\vartheta^k$ .

(iii) If  $\theta \in (\frac{1}{2}, 1)$ , then the sequence  $\{\mathcal{Z}^k\}$  converges R-sublinearly, i.e., there exists  $c > 0$  such that  $\|\mathcal{Z}^k - \mathcal{Z}^*\|_F \leq ck^{-\frac{1-\theta}{2\theta-1}}$ .

**Remark 9:** When the KL exponent of  $F$  in (5) can be computed, the detailed convergence rate of the proximal Gauss-Seidel algorithm can be obtained.

## V. NUMERICAL EXPERIMENTS

In this section, we conduct numerical experiments on several image datasets to verify the effectiveness and efficiency of the tensor factorization method via transformed tensor-tensor product (TFM-TTP) for image alignment, and compare with some state-of-the-art methods, including robust alignment by sparse and low-rank decomposition<sup>1</sup> (RASL) [2], transformed Grassmannian robust adaptive subspace tracking algorithm<sup>2</sup> (t-GRASTA) [11], nonconvex plus quadratic penalized low-rank and sparse decomposition (NQLSD) [15], alternating direction method of multipliers with  $\ell_p$  norm ( $\ell_p$ -ADMM) [22], and nonconvex image alignment by the low transformed multi-rank tensor plus sparsity (NCALTS) method [42]. All experiments are performed on MATLAB (R2018b) with an Intel Core i7-10750H 2.6GHz and 16GB RAM.

### A. Stopping Criteria

For the inner iterations of Algorithm 2, we adopt the distance  $\text{dist}(0, \partial F(\mathcal{X}^{k+1}, \mathcal{Y}^{k+1}, \mathcal{S}^{k+1}, \Delta\tau^{k+1}))$  to measure the accuracy of the optimal solution. However, it is hard to compute it directly. In light of Lemma 1(i) in Appendix C, we can find an upper bound of  $\text{dist}(0, \partial F(\mathcal{X}^{k+1}, \mathcal{Y}^{k+1}, \mathcal{S}^{k+1}, \Delta\tau^{k+1}))$  to stop Algorithm 2 in practice. Define  $\nu := \|\mathcal{V}_{\mathcal{X}}^{k+1} + \nabla_{\mathcal{X}} Q^{k+1}\|_F + \|\mathcal{V}_{\mathcal{Y}}^{k+1} + \nabla_{\mathcal{Y}} Q^{k+1}\|_F + \|\mathcal{V}_{\mathcal{S}}^{k+1} + \nabla_{\mathcal{S}} Q^{k+1}\|_F + \|\xi^k(\Delta\tau^k - \Delta\tau^{k+1})\|_F$ . Let  $\text{tol}$  be a given tolerance. Algorithm 2 will be terminated if

$$\frac{\nu}{1 + \|\mathcal{D} \circ \tau^t\|_F + \|\mathcal{X}^{k+1}\|_F + \|\mathcal{Y}^{k+1}\|_F + \|\mathcal{S}^{k+1}\|_F} \leq \text{tol},$$

or the maximum number of iterations reaches 200. In the experiments, we set  $\text{tol}$  to be  $1 \times 10^{-2}$  in all experiments except for the handwritten number “8” with mixed noise, which is set to be  $5 \times 10^{-2}$ .

For the outer iterations, we stop Algorithm 1 until the relative change of the value of the cost function between two consecutive iterations is smaller than  $1 \times 10^{-2}$ , or the maximum number of iterations reaches 60.

<sup>1</sup><http://people.eecs.berkeley.edu/~yima/matrix-rank/rasl.html>

<sup>2</sup><http://sites.google.com/site/hejunzz/t-grasta>

### B. Implementation Details

1) *Parameters setting:* As suggested by [38, Theorem 2] for robust tensor completion, we set  $\lambda = a/\sqrt{\max\{n_1, n_2\}n_3}$ , where  $a$  is chosen from the range  $[0.0005, 0.2]$  to get the best possible results. For the parameters  $\rho_i$ , we take them the same for different  $i = 1, 2, 3$ , which are chosen from the interval  $[0.01, 0.4]$  to get the best recovery images in all experiments. The parameters  $\alpha^k, \beta^k, \gamma^k, \xi^k$  of the proximal terms in Algorithm 2 are not sensitive to the results and we set  $\alpha^k = \beta^k = \gamma^k = \xi^k = 1 \times 10^{-5}$  in all experiments. For the parameter  $p$  in the tensor  $\ell_p$  norm of sparse noise, the recovery performance may be influenced for different image datasets, and we choose it from the set  $\{0.1, 0.25, 0.3, 0.4, 0.5, 0.6, 0.65, 0.7, 0.75\}$  to get the best recovery results in the experiments.

2) *Unitary transform matrix in U-product:* The selection of the unitary transform matrix  $\mathbf{U}$  in the transformed tensor-tensor product plays a vital role for TFM-TTP. Similar to [37]–[42], we adopt the following approach to obtain the data-dependent unitary matrix. First, we get an initial estimator  $\hat{\mathcal{L}}$  by model (2) based on the discrete cosine transform in the U-product. Then  $\hat{\mathcal{L}}$  is unfolded along the third dimension, i.e.,  $\hat{\mathcal{L}}_{(3)} = \mathbf{L}$ . Assume that the SVD of  $\mathbf{L}$  is given by  $\mathbf{L} = \bar{\mathbf{U}}\bar{\mathbf{\Sigma}}\bar{\mathbf{V}}^T$ . Then we choose  $\bar{\mathbf{U}}^T$  as the unitary matrix in the U-product. In this case, one can get lower transformed multi-rank of a tensor by using the data-dependent transformation. More details about the construction of the unitary matrix in the U-product can be found in [38], [41].

3) *Adaptive Transformed Multi-Rank Update:* For the transformed multi-rank of a tensor, we adopt an adaptive update strategy in the experiments. At the  $k$ th iteration of Algorithm 2, assume that the tensor  $\mathcal{L}^k \in \mathbb{R}^{n_1 \times n_2 \times n_3}$  is decomposed into the U-product of two smaller tensors  $\mathcal{L}^k = \mathcal{X}^k \diamond_{\mathbf{U}} \mathcal{Y}^k$ , where  $\mathcal{X}^k \in \mathbb{R}^{n_1 \times r \times n_3}$ ,  $\mathcal{Y}^k \in \mathbb{R}^{r \times n_2 \times n_3}$ , and  $r$  is the transformed tubal rank of  $\mathcal{L}^k$ . Similar to [33], [53], [54], the rank-decreasing scheme is adopted to estimate the transformed multi-rank of  $\mathcal{L}^{k+1}$ , whose details are given as follows.

First, suppose that the transformed multi-rank of  $\mathcal{L}^k$  is  $\mathbf{r}^k = (r_1^k, r_2^k, \dots, r_{n_3}^k)$ . The matrix  $(\hat{\mathcal{L}}_{\mathbf{U}}^k)^{(i)} \in \mathbb{R}^{n_1 \times n_2}$  is factorized into the product of two smaller matrices  $(\hat{\mathbf{X}}^k)^{(i)} \in \mathbb{R}^{n_1 \times r_i^k}$  and  $(\hat{\mathbf{Y}}^k)^{(i)} \in \mathbb{R}^{r_i^k \times n_2}$ . Second, we calculate the eigenvalues of  $((\hat{\mathbf{X}}^k)^{(i)})^T(\hat{\mathbf{X}}^k)^{(i)}$ ,  $i = 1, 2, \dots, n_3$ , and sort all eigenvalues of the  $n_3$  matrices, which are denoted by  $\lambda_1 \geq \lambda_2 \geq \dots \geq \lambda_{n_a}$ , where  $n_a = \sum_{i=1}^{n_3} r_i^k$ . Finally, we compute the quotients  $\hat{\lambda}_i = \frac{\lambda_i}{\lambda_{i+1}}$ ,  $i = 1, 2, \dots, n_a - 1$ .

Let the index of maximum  $\hat{\lambda}_i$  be  $m$ , i.e.,  $m = \text{argmax}_{1 \leq i \leq n_a - 1} \hat{\lambda}_i$ . Define

$$\text{gap} := \frac{(m-1)\hat{\lambda}_m}{\sum_{i \neq m} \hat{\lambda}_i}.$$

If  $\text{gap} \geq 10$ , it means that there exists a large drop in the magnitude of eigenvalues. Then one should reduce each entry of  $\mathbf{r}^k$ . Specifically, we find  $\lambda_{s^k}$  such that  $\sum_{i=1}^{s^k} \lambda_i / \sum_{i=1}^{n_a} \lambda_i \geq 95\%$ , where  $s^k$  is the corresponding index of  $\lambda_{s^k}$ . Suppose that there are  $d_i^k$  eigenvalues of  $((\hat{\mathbf{X}}^k)^{(i)})^T(\hat{\mathbf{X}}^k)^{(i)}$  belonging to  $\{\lambda_{s^k+1}, \dots, \lambda_{n_a}\}$ , then we set  $r_i^k = r_i^k - d_i^k$ . Let the skinny SVD of  $((\hat{\mathbf{X}}^k)^{(i)})^T(\hat{\mathbf{X}}^k)^{(i)}$  be  $\mathbf{U}^{(i)} \mathbf{\Sigma}^{(i)} (\mathbf{V}^{(i)})^T$ , then

TABLE 1

RECONSTRUCTION ERRORS AND CPU TIME (IN SECONDS) OF DIFFERENT METHODS FOR THE AR FACE DATABASE CORRUPTED BY SALT-AND-PEPPER IMPULSE NOISE WITH NOISE LEVEL 30%.

s	$\alpha$	RASL		t-GRASTA		NQLSD		$\ell_p$ -ADMM		NCALTS		TFM-TTP	
		error	time	error	time	error	time	error	time	error	time	error	time
3	3	0.1491	<u>6.11</u>	0.1465	54.35	0.1394	15.53	0.1377	145.64	0.1336	26.82	<b>0.1311</b>	<b>5.93</b>
	6	0.1524	13.40	0.1513	44.71	0.1403	<u>11.94</u>	0.1401	196.23	<u>0.1339</u>	38.51	<b>0.1326</b>	<b>6.15</b>
	9	0.1568	26.57	0.1531	63.74	0.1449	<u>17.13</u>	0.1459	205.85	<u>0.1366</u>	51.33	<b>0.1344</b>	<b>6.05</b>
5	3	0.1820	<u>6.47</u>	0.1811	69.13	0.1747	<b>5.31</b>	0.1775	48.10	0.1662	21.62	<b>0.1654</b>	6.51
	6	0.1847	<u>17.21</u>	0.1820	59.53	0.1770	19.92	0.1770	60.09	<u>0.1684</u>	31.97	<b>0.1681</b>	<b>17.00</b>
	9	0.1908	<u>26.29</u>	0.1907	51.19	0.1848	29.55	0.1814	53.43	<u>0.1749</u>	40.06	<b>0.1741</b>	<b>15.48</b>
7	3	0.1981	11.81	0.1971	19.29	0.1906	<b>5.67</b>	0.1930	48.28	0.1807	17.24	<b>0.1791</b>	10.89
	6	0.2035	24.02	0.2020	41.32	0.1961	<u>18.45</u>	0.1970	93.77	<u>0.1872</u>	33.52	<b>0.1866</b>	<b>17.00</b>
	9	0.2078	40.24	0.2048	80.87	<u>0.2003</u>	<u>9.42</u>	0.2029	47.38	<b>0.1895</b>	26.26	<b>0.1895</b>	<b>9.39</b>

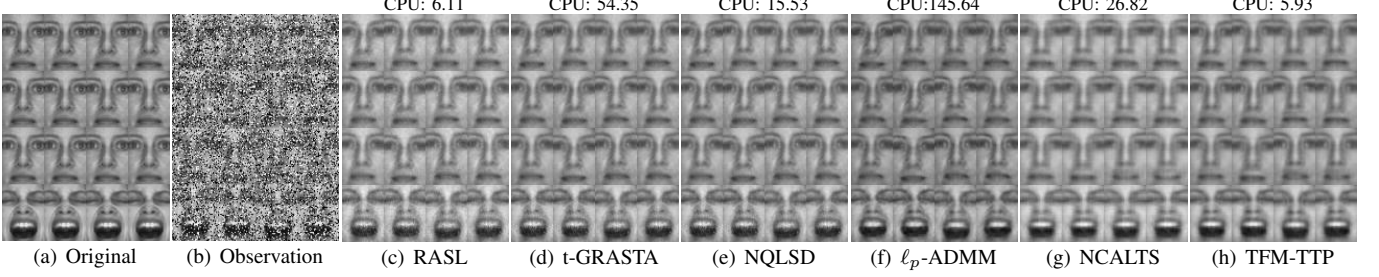


Fig. 1. Recovered images and CPU time (in seconds) of different methods for the AR Face database corrupted by salt-and-pepper impulse noise with noise level 30%, where  $s = 3, \alpha = 3$ .

TABLE 2

RECONSTRUCTION ERRORS AND CPU TIME (IN SECONDS) OF DIFFERENT METHODS FOR THE AR FACE DATABASE CORRUPTED BY SALT-AND-PEPPER IMPULSE NOISE WITH NOISE LEVEL 20% AND GAUSSIAN NOISE WITH ZERO-MEAN AND VARIANCE  $\sigma^2 = 0.01$ .

s	$\alpha$	RASL		t-GRASTA		NQLSD		$\ell_p$ -ADMM		NCALTS		TFM-TTP	
		error	time	error	time	error	time	error	time	error	time	error	time
3	3	0.1448	5.81	0.1383	83.97	0.1295	<u>5.56</u>	0.1271	29.84	<u>0.1248</u>	20.55	<b>0.1206</b>	<b>5.02</b>
	6	0.1468	12.81	0.1427	81.05	0.1342	<u>8.71</u>	0.1292	45.90	<u>0.1265</u>	42.38	<b>0.1231</b>	<b>8.30</b>
	9	0.1523	24.84	0.1512	80.88	0.1385	<u>13.77</u>	0.1353	32.01	<u>0.1295</u>	56.54	<b>0.1264</b>	<b>11.56</b>
5	3	0.1705	17.12	0.1693	221.99	0.1633	<u>10.15</u>	0.1639	38.22	<u>0.1541</u>	26.69	<b>0.1532</b>	<b>7.03</b>
	6	0.1754	18.03	0.1763	615.73	0.1665	<u>13.94</u>	0.1651	59.00	<u>0.1570</u>	33.67	<b>0.1567</b>	<b>7.46</b>
	9	0.1791	29.49	0.1798	108.36	0.1732	<u>27.49</u>	0.1714	36.99	<u>0.1616</u>	73.96	<b>0.1605</b>	<b>24.72</b>
7	3	0.1940	24.91	0.1945	40.80	0.1878	<u>15.56</u>	0.1894	24.55	<b>0.1777</b>	24.91	<u>0.1792</u>	<b>15.39</b>
	6	0.1991	<u>17.43</u>	0.1982	36.39	0.1925	<u>23.85</u>	0.1922	22.74	<u>0.1830</u>	37.38	<b>0.1829</b>	<b>15.17</b>
	9	0.2036	55.76	0.2049	37.64	0.1981	<u>31.94</u>	0.1972	52.91	<u>0.1899</u>	73.27	<b>0.1885</b>	<b>29.07</b>

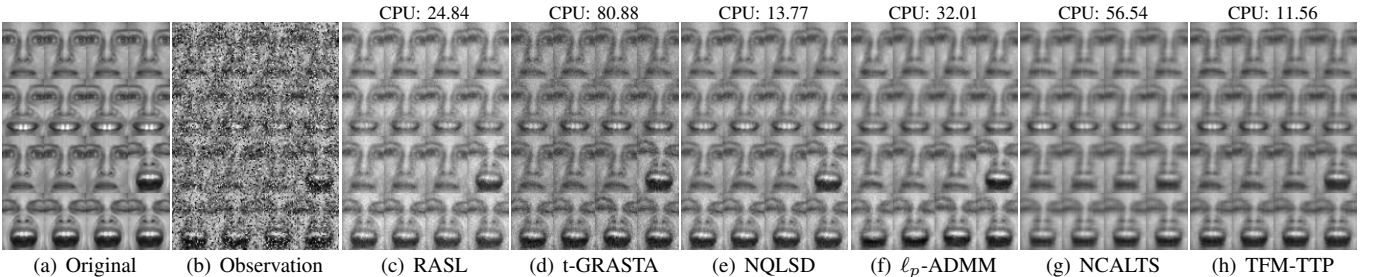


Fig. 2. Recovered images and CPU time (in seconds) of different methods for the AR Face database corrupted by salt-and-pepper impulse noise with noise level 20% and Gaussian noise with zero-mean and variance  $\sigma^2 = 0.01$ , where  $s = 3, \alpha = 9$ .

we update  $(\hat{\mathbf{X}}^k)^{(i)} = \mathbf{U}_{r_i^k}^{(i)} \Sigma_{r_i^k}^{(i)}$  and  $(\hat{\mathbf{Y}}^k)^{(i)} = (\mathbf{V}_{r_i^k}^{(i)})^T$ , where  $\mathbf{U}_{r_i^k}^{(i)}$  consists of the first  $r_i^k$  columns of  $\mathbf{U}^{(i)}$ ,  $\mathbf{V}_{r_i^k}^{(i)}$  consists of the first  $r_i^k$  rows of  $\mathbf{V}^{(i)}$ , and  $\Sigma_{r_i^k}^{(i)}$  is a diagonal matrix whose elements are the largest  $r_i^k$  diagonal elements of  $\Sigma^{(i)}$ .

### C. Image Alignment with Controlled Images

Table 1 reports the reconstruction errors and CPU time (in seconds) of different methods with different misaligned levels for the AR Face database corrupted by salt-and-pepper impulse noise with noise level 30%, where the boldface number is the best and the underline number is the second best. We can observe that the TFM-TTP performs better than RASL, t-GRASTA, NQLSD, and  $\ell_p$ -ADMM in terms of reconstruction errors for all cases. For  $s = 7$  and  $\alpha = 9$ , the reconstruction

In the experiments, we set the initial rank estimate  $\mathbf{r}^0$  to be  $[30, \dots, 30] \in \mathbb{R}^{n_3}$  for all testing datasets in Algorithm 2.

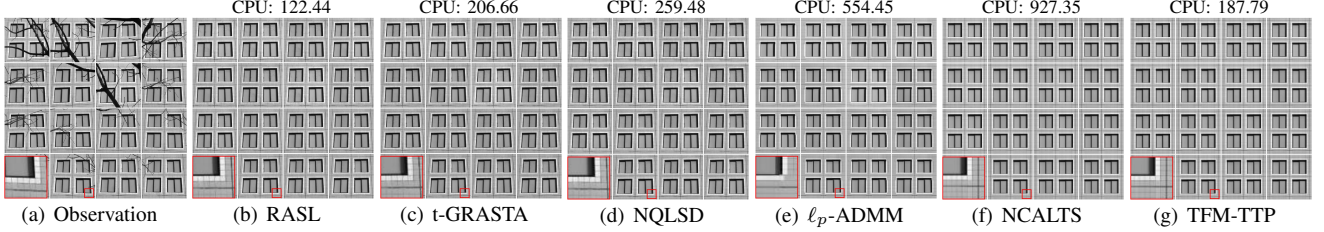


Fig. 3. Recovered images, zoomed regions, and CPU time (in seconds) of different methods for the windows dataset.

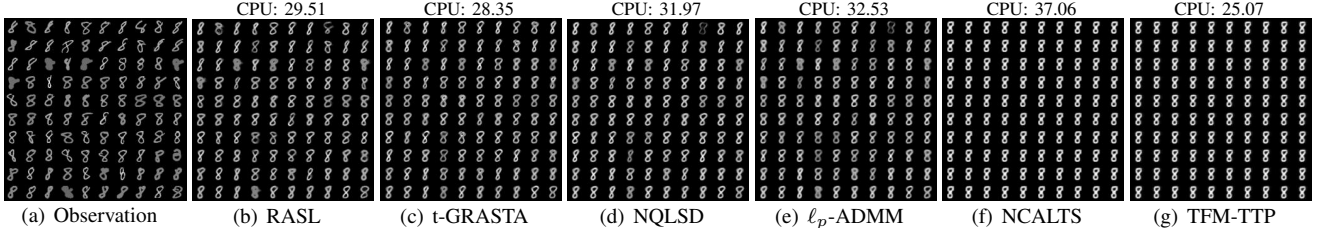


Fig. 4. Recovered images and CPU time (in seconds) of different methods for the handwritten digit “8”.

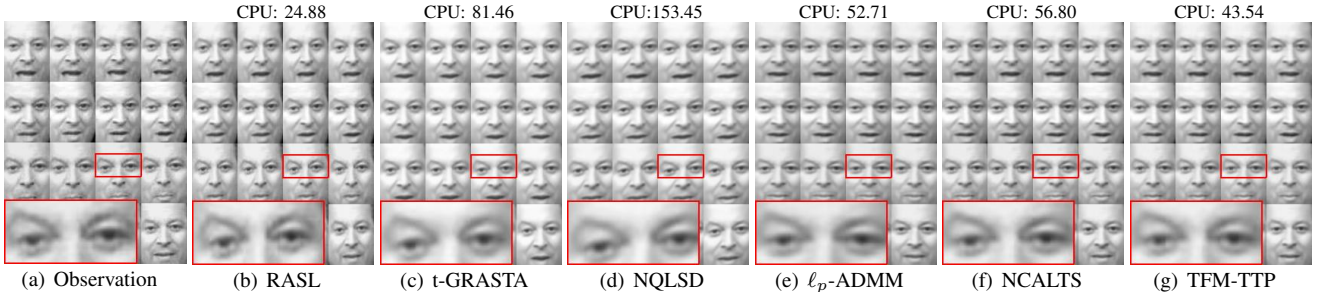


Fig. 5. Recovered images, zoomed regions, and CPU time (in seconds) of different methods for the AI Gore talking dataset.

error achieved by TFM-TTP is the same as that obtained by NCALTS. However, the CPU time (in seconds) required by NCALTS are much more than that required by TFM-TTP. Moreover, the NQLSD and  $\ell_p$ -ADMM perform better than RASL, which implies that the nonconvex matrix based methods are superior to the nuclear norm minimization method in terms of reconstruction errors. Although the CPU time required by NQLSD is small for few cases, the reconstruction errors of NQLSD are much larger than those of TFM-TTP.

In this subsection, we assess the effectiveness of TFM-TTP on the AR Face database<sup>3</sup> for image alignment, where the constructions of the images with misalignment are similar to [2], [22], [42]. First, we select 8 images from the AR Face database and resize them to  $80 \times 60$ . Second, for each image, we generate 15 images using the Euclidean transformation with uniformly distributed angles of rotation in the range  $[-\alpha/2, \alpha/2]$  degrees, and uniformly distributed  $x$ - and  $y$ -translations in the range  $[-s/2, s/2]$  pixels, where  $\alpha$  is selected from the set  $\{3, 6, 9\}$  and  $s$  is selected from the set  $\{3, 5, 7\}$  in the experiments. For the 120 images with misalignment, we add salt-and-pepper impulse noise with noise level 30%, or the mixed noise (salt-and-pepper impulse noise with noise level 20% and Gaussian noise with zero-mean and variance  $\sigma^2 = 0.01$ ). Since the rotation or translation in the Euclidean transformation may cause some pixels out of the image boundary, we crop each transformed and noisy image

with size  $50 \times 40$  in the center to construct the tensor  $\mathcal{D}$ . The reconstruction error is used to measure the accuracy of the recovered tensor, which is defined as  $\|\mathcal{L} - \mathcal{L}_0\|_F / \|\mathcal{L}_0\|_F$ . Here  $\mathcal{L}_0$  and  $\mathcal{L}$  are the ground-truth tensor and the recovered tensor, respectively. For each pair  $(\alpha, s)$ , we run 10 trials at random and take the average value of these results as the final result.

In Figure 1, we show the recovered images of different methods for the AR Face database corrupted by salt-and-pepper impulse noise with noise level 30%, where  $s = 3, \alpha = 3$ . We can see from this figure that the visual quality of the recovered images by TFM-TTP is better than that by RASL, t-GRASTA, NQLSD,  $\ell_p$ -ADMM, and NCALTS. In particular, the last rows of Figure 1 (c)-(h) show that the images recovered by TFM-TTP are more clear than those recovered by RASL, t-GRASTA, NQLSD,  $\ell_p$ -ADMM, and NCALTS, such as the regions of mouths. Moreover, the TFM-TTP can align the images better than RASL, t-GRASTA, and  $\ell_p$ -ADMM. And the CPU time required by TFM-TTP is much less than other compared methods.

Table 2 reports the reconstruction errors and CPU time (in seconds) of different methods for the AR Face database corrupted by salt-and-pepper impulse noise with noise level 20% and Gaussian noise with zero-mean and variance  $\sigma^2 = 0.01$  simultaneously, where the best results are highlighted in bold and the second best results are highlighted in underline. We can see that the reconstruction errors of NQLSD and  $\ell_p$ -ADMM are smaller than those of RASL and t-GRASTA

<sup>3</sup><http://www2.ece.ohio-state.edu/~aleix/ARdatabase.html>

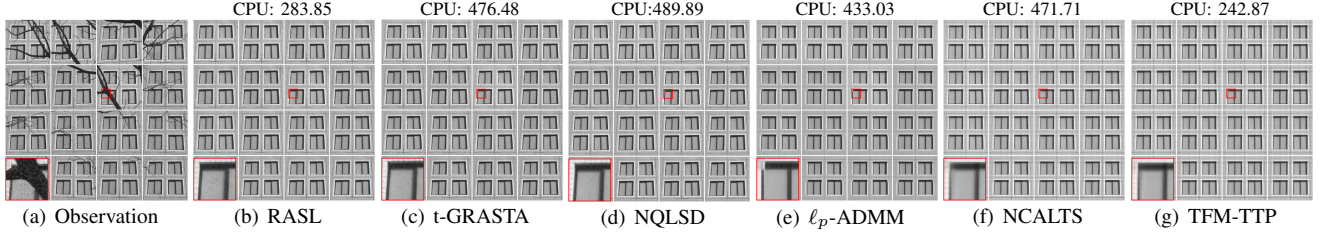


Fig. 6. Recovered images, zoomed regions, and CPU time (in seconds) of different methods for the window images corrupted by 20% salt-and-pepper impulse noise.

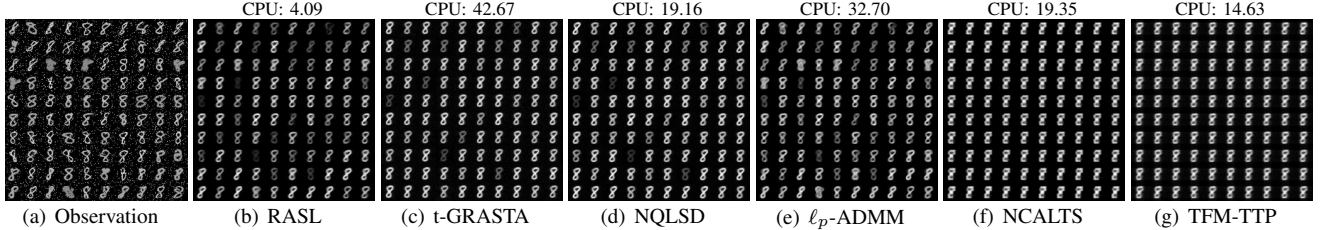


Fig. 7. Recovered images and CPU time (in seconds) of different methods for the handwritten digits “8” corrupted by 10% salt-and-pepper impulse noise.

for all cases. Moreover, the TFM-TTP outperforms RASL, t-GRASTA, NQLSD,  $\ell_p$ -ADMM, and NCALTS for most testing cases in terms of construction errors. And the computational time required by t-GRASTA is the most compared with other methods. Besides, the TFM-TTP is significantly faster than other compared methods at nearly the same (or lower) level of reconstruction errors.

Figure 2 shows the visual quality and CPU time (in seconds) comparisons of the recovered images of different methods for the AR Face database corrupted by salt-and-pepper impulse noise with noise level 20% and zero-mean Gaussian noise with variance  $\sigma^2 = 0.01$ , where  $s = 3, \alpha = 9$ . It can be seen that the images recovered by TFM-TTP are more clear than those recovered by RASL, t-GRASTA, NQLSD,  $\ell_p$ -ADMM, and NCALTS, which can be seen from the eyes and mouths of these images, e.g., the image in the second row and the first column. Moreover, the alignment of these images obtained by TFM-TTP is better than that obtained by RASL, t-GRASTA and NQLSD. Besides, the CPU time required by TFM-TTP is much less than that required by other compared methods for this case.

#### D. Image Alignment with Uncontrolled Images

In this subsection, we compare TFM-TTP with RASL, t-GRASTA, NQLSD,  $\ell_p$ -ADMM, NCALTS on three real-world image datasets, where there are no ground-truth images for comparisons. Here the original images are misaligned and corrupted by sparse noise. The first image dataset (windows) includes 16 images of the side of a building [2], which are taken by a personal camera from different viewpoints. The 16 images have some occlusions due to the tree branches, and the size of each image is  $1200 \times 1600$ . We crop these images to  $200 \times 200$  in the center and then the size of the resulting tensor is  $200 \times 200 \times 16$ . The second dataset contains 100 images of handwritten digit “8” taken from the MNIST dataset<sup>4</sup>, which are misaligned due to the different characteristic of the

handwritten digit. We use 100 images with size  $29 \times 29$  and then the resulting tensor is  $29 \times 29 \times 100$ . The third dataset is the Al Gore talking [2], which contains 140 frames with size of each image being  $80 \times 60$  and are misaligned by a significant jitter of the detector from frame to frame. Then the size of resulting tensor is  $80 \times 60 \times 140$ . To demonstrate the effectiveness of our proposed TFM-TTP method, we conduct three experiments in the following subsections: (1) Recover the natural images; (2) Recover the natural images with salt-and-pepper impulse noise; (3) Recover the natural images with salt-and-pepper impulse noise and Gaussian noise.

1) *Natural Images*: In this subsection, we show the recovery and alignment performance of different methods for the three real-world natural images in Figures 3-5. In Figure 3, the visual comparisons and zoomed regions of different methods are shown for the windows dataset. It can be seen that the alignment performance of NCALTS and TFM-TTP are better than that of RASL, t-GRASTA, NQLSD, and  $\ell_p$ -ADMM, especially for the zoomed regions of these images. Moreover, the images recovered by TFM-TTP are more clear than those recovered by other methods. The details of texture of the zoomed regions of TFM-TTP are kept better than those of RASL, t-GRASTA, NQLSD,  $\ell_p$ -ADMM, and NCALTS, where the TFM-TTP preserves sharp edges of the images better. For the computational time, the RASL requires less CPU time than other methods. While its recovery performance is not good in terms of alignment and visual quality. However, the computational time required by TFM-TTP is much less than that required by t-GRASTA, NQLSD,  $\ell_p$ -ADMM, and NCALTS. In particular, the recovery performance of TFM-TTP is slightly better than that of NCALTS, while the TFM-TTP is much faster than NCALTS.

In Figure 4, we show the recovered images and CPU time (in seconds) of different methods for the handwritten number “8”. It can be seen that the alignment performance and recovered images of NCALTS and TFM-TTP are much better than those of RASL, t-GRASTA, NQLSD, and  $\ell_p$ -ADMM. Compared with NCALTS, the TFM-TTP can align

<sup>4</sup><http://yann.lecun.com/exdb/mnist/>

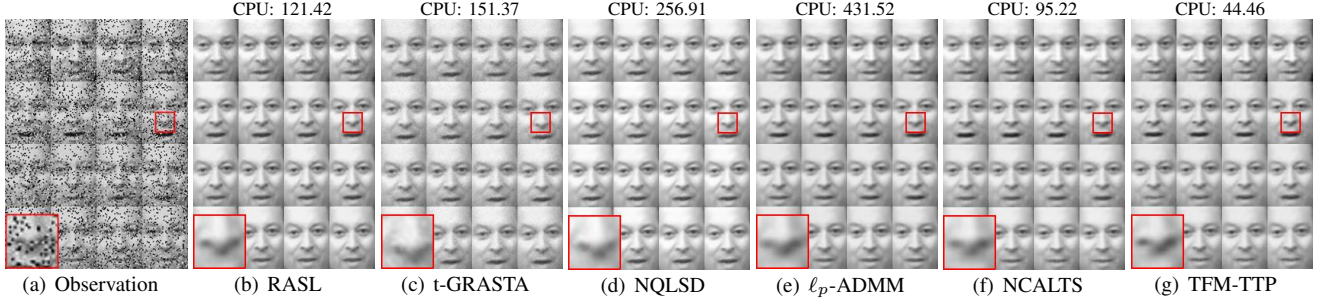


Fig. 8. Recovered images, zoomed regions, and CPU time (in seconds) of different methods for the AI Gore talking dataset corrupted by 20% salt-and-pepper impulse noise.

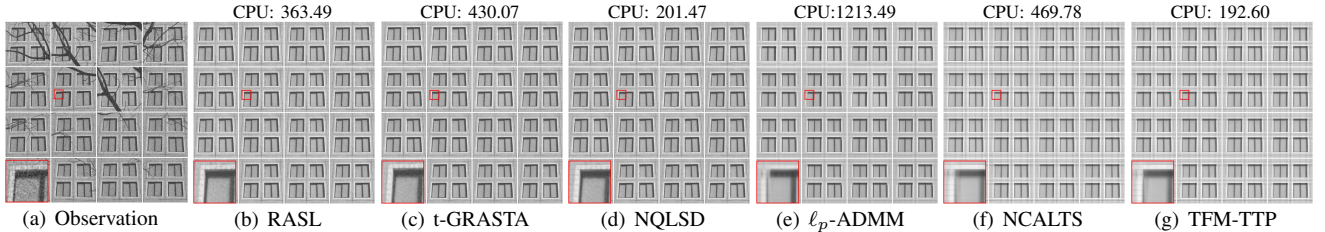


Fig. 9. Recovered images, zoomed regions, and CPU time (in seconds) of different methods for the window images corrupted by salt-and-pepper impulse noise with noise level 30% and zero-mean Gaussian noise with variance  $\sigma^2 = 0.05$ .

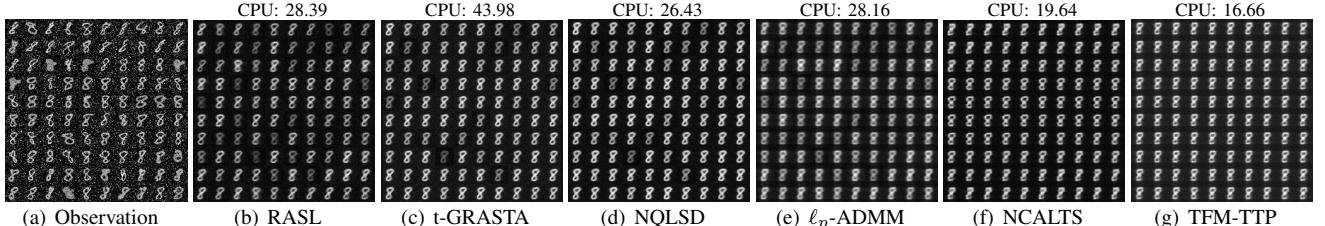


Fig. 10. Recovered images and CPU time (in seconds) of different methods for the handwritten digits “8” corrupted by salt-and-pepper impulse noise with noise level 10% and zero-mean Gaussian noise with variance  $\sigma^2 = 0.05$ .

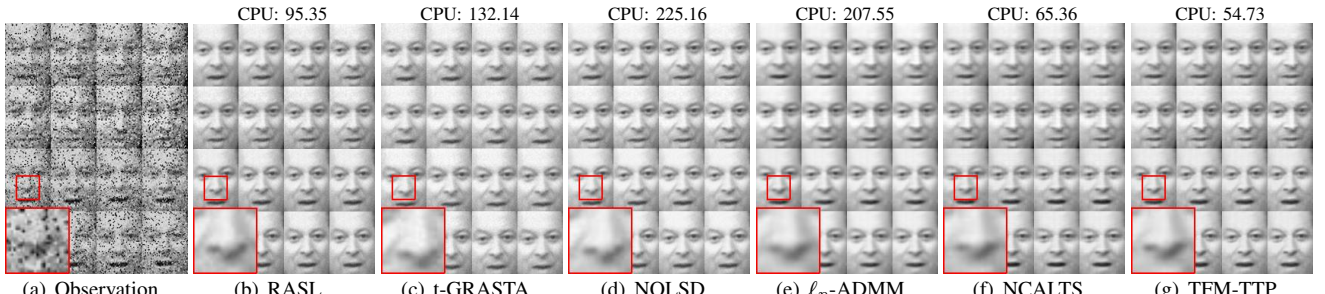


Fig. 11. Recovered images, zoomed regions, and CPU time (in seconds) of different methods for the AI Gore talking dataset corrupted by salt-and-pepper impulse noise with noise level 15% and zero-mean Gaussian noise with variance  $\sigma^2 = 0.05$ .

these images slightly better, see the third row and last column of the figure. Moreover, the CPU time required by TFM-TTP is less than that required by other methods.

Figure 5 shows the visual comparisons, zoomed regions, and CPU time (in seconds) of the AI Gore talking dataset recovered by different methods. It can be seen from the zoomed regions of these images that the alignment performance of  $\ell_p$ -ADMM, NCALTS, and TFM-TTP is much better than that of RASL, t-GRASTA, and NQLSD, which is shown by eyes of the zoomed regions. Moreover, the TFM-TTP outperforms  $\ell_p$ -ADMM and NCALTS in terms of the visual quality. Although the CPU time of RASL is much less than that of other methods, the recovery and alignment performance of images of RASL are much worse than that of NCALTS and TFM-TTP.

Besides, the TFM-TTP takes less CPU time than NCALTS since computing the SVDs of the frontal slices of a tensor is much expensive than the transformed tensor-tensor product.

2) *Natural Images with Salt-and-Pepper Impulse Noise*: In this subsection, we show the performance of different methods for the three real-world image datasets corrupted by salt-and-pepper impulse noise in Figures 6-8. Figure 6 shows the recovered images, zoomed regions, and CPU time (in seconds) of different methods for the natural window images corrupted by salt-and-pepper impulse noise with noise level 20%. It can be seen that the images recovered by  $\ell_p$ -ADMM, NCALTS, and TFM-TTP are aligned better than those recovered by RASL, t-GRASTA, and NQLSD. Moreover, the recovered images of TFM-TTP are more clear than those of RASL,

t-GRASTA, NQLSD,  $\ell_p$ -ADMM, and NCALTS, which can be seen from the left upper corners of the zoomed regions. Furthermore, the CPU time required by TFM-TTP is much less than that required by other compared methods.

In Figure 7, we show the recovered images and CPU time (in seconds) of different methods for the handwritten digits “8” corrupted by salt-and-pepper impulse noise with noise level 10%. It can be observed that the images recovered by TFM-TTP are more clear than those recovered by RASL, t-GRASTA, NQLSD,  $\ell_p$ -ADMM, and NCALTS. Some handwritten digits “8” are missing for the RASL, t-GRASTA, NQLSD, and  $\ell_p$ -ADMM. Moreover, NCALTS and TFM-TTP perform much better than RASL, t-GRASTA, NQLSD, and  $\ell_p$ -ADMM in terms of image alignment performance. Although the CPU time required by RASL is less than that required by TFM-TTP, its recovery quality is much worse than that of TFM-TTP. In addition, the TFM-TTP requires less CPU time than t-GRASTA, NQLSD,  $\ell_p$ -ADMM, and NCALTS.

Figure 8 shows the recovered images, zoomed regions, and CPU time (in seconds) of different methods for the AI Gore talking dataset corrupted by 20% salt-and-pepper impulse noise. We can see from this figure that the images obtained by TFM-TTP are more clear than those obtained by RASL, t-GRASTA, NQLSD,  $\ell_p$ -ADMM, and NCALTS, especially for the zoomed regions of these images, where the nose of TFM-TTP keeps more details than those of other methods. Besides, the alignment performance of  $\ell_p$ -ADMM, NCALTS, TFM-TTP is better than that of RASL, t-GRASTA, and NQLSD. And the CPU time required by TFM-TTP is much less than that required by other compared methods.

3) *Natural Images with Mixed Noise*: In this subsection, we show the recovery and alignment performance of different methods for the three real-world image datasets in Figures 9–11, which are corrupted by salt-and-pepper impulse noise and additive Gaussian noise simultaneously. Figure 9 shows the recovered images, zoomed regions, and CPU time (in seconds) of different methods for the window images corrupted by salt-and-pepper impulse noise with noise level 30% and zero-mean Gaussian noise with variance  $\sigma^2 = 0.05$ . It can be seen that the  $\ell_p$ -ADMM, NCALTS, and TFM-TTP can align the images better than RASL, t-GRASTA, and NQLSD. And the images recovered by TFM-TTP are more clear than those recovered by RASL, t-GRASTA, NQLSD,  $\ell_p$ -ADMM, and NCALTS, which can be seen from the zoomed regions of these images. Furthermore, the CPU time required by TFM-TTP is much less than that required by other compared methods.

In Figure 10, we show the recovered images and CPU time (in seconds) of different methods for the handwritten digits images corrupted by salt-and-pepper impulse noise with noise level 10% and zero-mean Gaussian noise with variance  $\sigma^2 = 0.05$ . It can be observed that the images recovered by TFM-TTP are more clear than those recovered by RASL, t-GRASTA, NQLSD,  $\ell_p$ -ADMM, and NCALTS. Some handwritten digits images obtained by the RASL, t-GRASTA, NQLSD, and  $\ell_p$ -ADMM are missing. Moreover, the alignment of TFM-TTP is better than that of other methods. And the computational time of TFM-TTP is much less than that of RASL, t-GRASTA, NQLSD,  $\ell_p$ -ADMM, and NCALTS.

Figure 11 shows the recovered images, zoomed regions, and CPU time (in seconds) of different methods for the AI Gore talking dataset corrupted by salt-and-pepper impulse noise with noise level 15% and zero-mean Gaussian noise with variance  $\sigma^2 = 0.05$ . We can see from this figure that the zoomed regions of images recovered by TFM-TTP are much more clear than those recovered by RASL, t-GRASTA, NQLSD,  $\ell_p$ -ADMM, and NCALTS, where the nose of the zoomed region of TFM-TTP is more clear than those of other compared methods. Furthermore, the alignment of images obtained by NCALTS and TFM-TTP is better than that obtained by RASL, t-GRASTA, NQLSD, and  $\ell_p$ -ADMM, e.g., see the first images of these images. Besides, the CPU time required by TFM-TTP is much less than that required by other compared methods.

## VI. CONCLUDING REMARKS

In this paper, we have proposed a low-rank tensor factorization method based on transformed tensor-tensor product for aligning a batch of linearly correlated images, where the observed images are deformed by some unknown domain transformations and corrupted by sparse noise and Gaussian noise simultaneously. By stacking these images as the frontal slices of a third-order tensor, the observed tensor after domain transformations can be decomposed into the sum of a low-rank tensor, a sparse tensor, and a noisy tensor with Gaussian distribution. Then we propose to factorize the underlying tensor into the U-product of two smaller tensors under any unitary transformation to explore its low-rankness, whose computation is much cheaper than that of the transformed tensor nuclear norm since one needs to perform the SVDs of a series of matrices in the transformed tensor nuclear norm. Furthermore, the tensor  $\ell_p$  norm ( $0 < p < 1$ ) and the tensor Frobenius norm are employed to characterize the sparsity of the sparse noise and the distribution of Gaussian noise, respectively. A generalized Gauss-Newton algorithm is adopted to solve the proposed model via linearizing the domain transformations, where a proximal Gauss-Seidel algorithm is adapted to solve the resulting subproblem. The convergence and convergence rate of the proximal Gauss-Seidel algorithm are established under very mild conditions. Numerical examples on many image datasets have shown the effectiveness and efficiency of our TFM-TTP method when compared to other existing methods.

A future research topic is to establish the convergence of the generalized Gauss-Newton algorithm for solving our nonconvex model. Moreover, it is also interesting to analyze the error bound of the proposed model in future work (cf. [22], [42], [55]).

## ACKNOWLEDGEMENTS

The authors are grateful to Dr. Xiai Chen and Prof. Xiaoqin Zhang for sharing the codes of NQLSD [15] and  $\ell_q$ -ADMM [22], respectively. The authors are also grateful to Prof. Di Wang for helpful discussions about the geometric transformation in image alignment.

## APPENDIX A

In this section, we give the definitions of the subdifferential and the Kurdyka-Łojasiewicz (KL) property of a function, respectively, which play a vital role for establishing the convergence and rate of convergence of the proximal Gauss-Seidel algorithm.

*Definition 8:* [56, Definition 8.3] Consider a function  $f : \mathbb{R}^n \rightarrow (\infty, +\infty]$  and a point  $\bar{x}$  with  $f(\bar{x})$  finite. For any  $x \in \mathbb{R}^n$ , one says that

(i)  $v$  is a regular subgradient of  $f$  at  $\bar{x}$ , written as  $v \in \partial f(\bar{x})$ , if

$$\liminf_{x \rightarrow \bar{x}, x \neq \bar{x}} \frac{f(x) - f(\bar{x}) - \langle v, x - \bar{x} \rangle}{\|x - \bar{x}\|} \geq 0.$$

(ii)  $v$  is a subgradient of  $f$  at  $\bar{x}$ , written as  $v \in \partial f(\bar{x})$ , if there are sequences  $x^k \rightarrow \bar{x}$ ,  $f(x^k) \rightarrow f(\bar{x})$ , and  $v^k \in \partial f(x^k)$  with  $v^k \rightarrow v$ .

*Definition 9:* [52, Definition 2.1] Let  $f : \mathbb{R}^n \rightarrow \mathbb{R} \cup \{+\infty\}$  be a proper lower semicontinuous function. We say that  $f$  has the Kurdyka-Łojasiewicz (KL) property at point  $x^* \in \text{dom}(\partial f)$ , if there exist a neighborhood  $U$  of  $x^*$ ,  $\eta \in (0, +\infty]$  and a continuous concave function  $\varphi : [0, \eta) \rightarrow \mathbb{R}_+$  such that: (i)  $\varphi(0) = 0$ ; (ii)  $\varphi$  is  $C^1$  on  $(0, \eta)$ ; (iii) for all  $s \in (0, \eta)$ ,  $\varphi'(s) > 0$ ; (iv) and for all  $x$  in  $U \cap [f(x^*) < f < f(x^*) + \eta]$  the KL inequality holds:

$$\varphi'(f(x) - f(x^*)) \text{dist}(0, \partial f(x)) \geq 1. \quad (20)$$

If  $f$  satisfies the KL property at  $x^* \in \text{dom}(\partial f)$ , and the  $\varphi(s)$  in (20) can be chosen as  $\varphi(s) = \hat{c}s^{1-\theta}$  for some  $\hat{c} > 0$  and  $\theta \in [0, 1)$ , then we say that  $f$  satisfies the KL property at point  $x^*$  with exponent  $\theta$ .

A proper closed function  $f$  satisfying the KL property at every point in  $\text{dom}(\partial f)$  is said to be a KL function, and a proper closed function  $f$  satisfying the KL property with exponent  $[0, 1)$  at every point in  $\text{dom}(\partial f)$  is said to be a KL function with exponent  $\theta$  [52].

## APPENDIX B. PROOF OF THEOREM 1

It follows from (7), (8), (9) and (10) that

$$\left\{ \begin{array}{l} F(\mathcal{X}^{k+1}, \mathcal{Y}^k, \mathcal{S}^k, \Delta\tau^k) + \frac{\alpha^k}{2} \|\mathcal{X}^{k+1} - \mathcal{X}^k\|_F^2 \\ \leq F(\mathcal{X}^k, \mathcal{Y}^k, \mathcal{S}^k, \Delta\tau^k), \\ F(\mathcal{X}^{k+1}, \mathcal{Y}^{k+1}, \mathcal{S}^k, \Delta\tau^k) + \frac{\beta^k}{2} \|\mathcal{Y}^{k+1} - \mathcal{Y}^k\|_F^2 \\ \leq F(\mathcal{X}^{k+1}, \mathcal{Y}^k, \mathcal{S}^k, \Delta\tau^k), \\ F(\mathcal{X}^{k+1}, \mathcal{Y}^{k+1}, \mathcal{S}^{k+1}, \Delta\tau^k) + \frac{\gamma^k}{2} \|\mathcal{S}^{k+1} - \mathcal{S}^k\|_F^2 \\ \leq F(\mathcal{X}^{k+1}, \mathcal{Y}^{k+1}, \mathcal{S}^k, \Delta\tau^k), \\ F(\mathcal{X}^{k+1}, \mathcal{Y}^{k+1}, \mathcal{S}^{k+1}, \Delta\tau^{k+1}) + \frac{\xi^k}{2} \|\Delta\tau^{k+1} - \Delta\tau^k\|_F^2 \\ \leq F(\mathcal{X}^{k+1}, \mathcal{Y}^{k+1}, \mathcal{S}^{k+1}, \Delta\tau^k). \end{array} \right. \quad (21)$$

Summing the inequalities in (21) to obtain that

$$\begin{aligned} F(\mathcal{X}^{k+1}, \mathcal{Y}^{k+1}, \mathcal{S}^{k+1}, \Delta\tau^{k+1}) &+ \frac{\alpha^k}{2} \|\mathcal{X}^{k+1} - \mathcal{X}^k\|_F^2 \\ &+ \frac{\beta^k}{2} \|\mathcal{Y}^{k+1} - \mathcal{Y}^k\|_F^2 + \frac{\gamma^k}{2} \|\mathcal{S}^{k+1} - \mathcal{S}^k\|_F^2 \\ &+ \frac{\xi^k}{2} \|\Delta\tau^{k+1} - \Delta\tau^k\|_F^2 \leq F(\mathcal{X}^k, \mathcal{Y}^k, \mathcal{S}^k, \Delta\tau^k). \end{aligned} \quad (22)$$

Moreover, the optimality conditions of (7), (8), (9) and (10) yield

$$\left\{ \begin{array}{l} 0 = \nabla_{\mathcal{X}} Q(\mathcal{X}^{k+1}, \mathcal{Y}^k, \mathcal{S}^k, \Delta\tau^k) \\ \quad + \rho_1 \mathcal{X}^{k+1} + \alpha^k (\mathcal{X}^{k+1} - \mathcal{X}^k), \\ 0 = \nabla_{\mathcal{Y}} Q(\mathcal{X}^{k+1}, \mathcal{Y}^{k+1}, \mathcal{S}^k, \Delta\tau^k) \\ \quad + \rho_2 \mathcal{Y}^{k+1} + \beta^k (\mathcal{Y}^{k+1} - \mathcal{Y}^k), \\ 0 \in \nabla_{\mathcal{S}} Q(\mathcal{X}^{k+1}, \mathcal{Y}^{k+1}, \mathcal{S}^{k+1}, \Delta\tau^k) \\ \quad + \partial(\lambda \|\mathcal{S}^{k+1}\|_p^p) + \gamma^k (\mathcal{S}^{k+1} - \mathcal{S}^k), \\ 0 = \nabla_{\Delta\tau} Q(\mathcal{X}^{k+1}, \mathcal{Y}^{k+1}, \mathcal{S}^{k+1}, \Delta\tau^{k+1}) \\ \quad + \rho_3 \Delta\tau^{k+1} + \xi^k (\Delta\tau^{k+1} - \Delta\tau^k). \end{array} \right. \quad (23)$$

Let

$$\begin{aligned} \mathcal{V}_{\mathcal{X}}^{k+1} &:= -\nabla_{\mathcal{X}} Q(\mathcal{X}^{k+1}, \mathcal{Y}^k, \mathcal{S}^k, \Delta\tau^k) - \alpha^k (\mathcal{X}^{k+1} - \mathcal{X}^k), \\ \mathcal{V}_{\mathcal{Y}}^{k+1} &:= -\nabla_{\mathcal{Y}} Q(\mathcal{X}^{k+1}, \mathcal{Y}^{k+1}, \mathcal{S}^k, \Delta\tau^k) - \beta^k (\mathcal{Y}^{k+1} - \mathcal{Y}^k), \\ \mathcal{V}_{\mathcal{S}}^{k+1} &:= -\nabla_{\mathcal{S}} Q(\mathcal{X}^{k+1}, \mathcal{Y}^{k+1}, \mathcal{S}^{k+1}, \Delta\tau^k) - \gamma^k (\mathcal{S}^{k+1} - \mathcal{S}^k), \\ \mathcal{V}_{\Delta\tau}^{k+1} &:= -\nabla_{\Delta\tau} Q(\mathcal{X}^{k+1}, \mathcal{Y}^{k+1}, \mathcal{S}^{k+1}, \Delta\tau^{k+1}) \\ &\quad - \xi^k (\Delta\tau^{k+1} - \Delta\tau^k). \end{aligned} \quad (24)$$

Combining (23) and (24), we obtain that

$$\begin{aligned} \mathcal{V}_{\mathcal{X}}^{k+1} &= \rho_1 \mathcal{X}^{k+1}, & \mathcal{V}_{\mathcal{Y}}^{k+1} &= \rho_2 \mathcal{Y}^{k+1}, \\ \mathcal{V}_{\mathcal{S}}^{k+1} &\in \partial(\lambda \|\mathcal{S}^{k+1}\|_p^p), & \mathcal{V}_{\Delta\tau}^{k+1} &= \rho_3 \Delta\tau^{k+1}. \end{aligned} \quad (25)$$

Notice that  $0 < \underline{d} < \bar{d} < +\infty$  and  $\underline{d} \leq \alpha^k, \beta^k, \gamma^k, \xi^k \leq \bar{d}$ . Therefore, the sequence  $\{(\mathcal{X}^k, \mathcal{Y}^k, \mathcal{S}^k, \Delta\tau^k)\}$  satisfies

$$\left\{ \begin{array}{l} \|\nabla_{\mathcal{X}} Q(\mathcal{X}^{k+1}, \mathcal{Y}^k, \mathcal{S}^k, \Delta\tau^k) + \mathcal{V}_{\mathcal{X}}^{k+1}\|_F \\ \leq \bar{d} \|\mathcal{X}^{k+1} - \mathcal{X}^k\|_F, \\ \|\nabla_{\mathcal{Y}} Q(\mathcal{X}^{k+1}, \mathcal{Y}^{k+1}, \mathcal{S}^k, \Delta\tau^k) + \mathcal{V}_{\mathcal{Y}}^{k+1}\|_F \\ \leq \bar{d} \|\mathcal{Y}^{k+1} - \mathcal{Y}^k\|_F, \\ \|\nabla_{\mathcal{S}} Q(\mathcal{X}^{k+1}, \mathcal{Y}^{k+1}, \mathcal{S}^{k+1}, \Delta\tau^k) + \mathcal{V}_{\mathcal{S}}^{k+1}\|_F \\ \leq \bar{d} \|\mathcal{S}^{k+1} - \mathcal{S}^k\|_F, \\ \|\nabla_{\Delta\tau} Q(\mathcal{X}^{k+1}, \mathcal{Y}^{k+1}, \mathcal{S}^{k+1}, \Delta\tau^{k+1}) + \mathcal{V}_{\Delta\tau}^{k+1}\|_F \\ \leq \bar{d} \|\Delta\tau^{k+1} - \Delta\tau^k\|_F. \end{array} \right. \quad (26)$$

Furthermore, it follows from [44, Example 4] that the  $\ell_p$  norm ( $p > 0$ ) is a semi-algebraic function when  $p$  is rational. In particular, when  $p$  is taken to be 2, the  $\ell_p$  norm is just the tensor Frobenius norm. As a consequence,  $F(\mathcal{X}, \mathcal{Y}, \mathcal{S}, \Delta\tau)$  in (5) is a semi-algebraic function [44, Example 2]. Note that  $F(\mathcal{X}, \mathcal{Y}, \mathcal{S}, \Delta\tau)$  is proper and continuous. Then we can get that  $F(\mathcal{X}, \mathcal{Y}, \mathcal{S}, \Delta\tau)$  is a KL function [44, Theorem 3].

By the definition of  $F(\mathcal{X}, \mathcal{Y}, \mathcal{S}, \Delta\tau)$  in (5), one can easily obtain that  $F(\mathcal{X}, \mathcal{Y}, \mathcal{S}, \Delta\tau)$  is bounded from below

and tends to infinity as  $\|(\mathcal{X}, \mathcal{Y}, \mathcal{S}, \Delta\tau)\|_F$  tends to infinity. Hence, we can deduce that  $F(\mathcal{X}, \mathcal{Y}, \mathcal{S}, \Delta\tau)$  is coercive. Now we show that the sequence  $\{(\mathcal{X}^k, \mathcal{Y}^k, \mathcal{S}^k, \Delta\tau^k)\}$  generated by Algorithm 2 is bounded. Assume that the sequence  $\{(\mathcal{X}^k, \mathcal{Y}^k, \mathcal{S}^k, \Delta\tau^k)\}$  is unbounded, there exists a subsequence  $\{(\mathcal{X}^{k_i}, \mathcal{Y}^{k_i}, \mathcal{S}^{k_i}, \Delta\tau^{k_i})\}$ , which tends to infinity as  $i$  tends to infinity. By the coercivity of  $F$ , we obtain that  $F(\mathcal{X}^{k_i}, \mathcal{Y}^{k_i}, \mathcal{S}^{k_i}, \Delta\tau^{k_i})$  tends to infinity as  $i$  tends to infinity, which is contradictory to (22). Therefore, we get that the sequence  $\{(\mathcal{X}^k, \mathcal{Y}^k, \mathcal{S}^k, \Delta\tau^k)\}$  is bounded. It follows from [48, Theorem 6.2] that the desired conclusion is attained.

### APPENDIX C. PROOF OF THEOREM 2

*Lemma 1:* Let  $\{\mathcal{Z}^k\}$  be a sequence generated by Algorithm 2, whose limit point is denoted by  $\mathcal{Z}^*$ . Suppose that  $p$  is rational. Then the following statements hold:

(i) There exists a constant  $C > 0$  such that

$$\text{dist}(0, \partial F(\mathcal{Z}^{k+1})) \leq C \|\mathcal{Z}^{k+1} - \mathcal{Z}^k\|_F.$$

(ii) There exist  $\rho > 0$ ,  $\mu > 0$  and a KL exponent  $\theta \in [0, 1)$  of  $F$  such that

$$\begin{aligned} & \sum_{j=k}^{\infty} \|\mathcal{Z}^{j+1} - \mathcal{Z}^j\|_F \\ & \leq \|\mathcal{Z}^k - \mathcal{Z}^{k-1}\|_F + \frac{\mu}{\rho(1-\theta)} (F(\mathcal{Z}^k) - F(\mathcal{Z}^*))^{1-\theta}. \end{aligned} \quad (27)$$

(iii) We have  $\sum_{k=0}^{\infty} \|\mathcal{Z}^{k+1} - \mathcal{Z}^k\|_F < +\infty$ , hence  $\lim_{k \rightarrow \infty} \|\mathcal{Z}^{k+1} - \mathcal{Z}^k\|_F = 0$ .

(iv) For any positive integer  $k$ , it holds that

$$\sum_{j=k}^{\infty} \|\mathcal{Z}^{j+1} - \mathcal{Z}^j\|_F \geq \|\mathcal{Z}^k - \mathcal{Z}^*\|_F. \quad (28)$$

*Proof:* (i) The subdifferential of (5) at the  $(k+1)$ th iteration yields

$$\left\{ \begin{array}{l} \rho_1 \mathcal{X}^{k+1} + \nabla_{\mathcal{X}} Q(\mathcal{X}^{k+1}, \mathcal{Y}^{k+1}, \mathcal{S}^{k+1}, \Delta\tau^{k+1}) \\ \quad = \nabla_{\mathcal{X}} F(\mathcal{X}^{k+1}, \mathcal{Y}^{k+1}, \mathcal{S}^{k+1}, \Delta\tau^{k+1}), \\ \rho_2 \mathcal{Y}^{k+1} + \nabla_{\mathcal{Y}} Q(\mathcal{X}^{k+1}, \mathcal{Y}^{k+1}, \mathcal{S}^{k+1}, \Delta\tau^{k+1}) \\ \quad = \nabla_{\mathcal{Y}} F(\mathcal{X}^{k+1}, \mathcal{Y}^{k+1}, \mathcal{S}^{k+1}, \Delta\tau^{k+1}), \\ \mathcal{S}_1^{k+1} + \nabla_{\mathcal{S}} Q(\mathcal{X}^{k+1}, \mathcal{Y}^{k+1}, \mathcal{S}^{k+1}, \Delta\tau^{k+1}) \\ \quad \in \partial_{\mathcal{S}} F(\mathcal{X}^{k+1}, \mathcal{Y}^{k+1}, \mathcal{S}^{k+1}, \Delta\tau^{k+1}), \\ \rho_3 \Delta\tau^{k+1} + \nabla_{\Delta\tau} Q(\mathcal{X}^{k+1}, \mathcal{Y}^{k+1}, \mathcal{S}^{k+1}, \Delta\tau^{k+1}) \\ \quad = \nabla_{\Delta\tau} F(\mathcal{X}^{k+1}, \mathcal{Y}^{k+1}, \mathcal{S}^{k+1}, \Delta\tau^{k+1}), \end{array} \right.$$

where  $\mathcal{S}_1^{k+1} \in \partial(\lambda \|\mathcal{S}^{k+1}\|_p^p)$  and  $Q$  is defined as (6). Let  $Q^{k+1} = Q(\mathcal{X}^{k+1}, \mathcal{Y}^{k+1}, \mathcal{S}^{k+1}, \Delta\tau^{k+1})$ . Then, by [51, Proposition 2.1], we get that

$$\begin{aligned} w^{k+1} &:= (\rho_1 \mathcal{X}^{k+1} + \nabla_{\mathcal{X}} Q^{k+1}, \rho_2 \mathcal{Y}^{k+1} + \nabla_{\mathcal{Y}} Q^{k+1}, \\ &\quad \mathcal{S}_1^{k+1} + \nabla_{\mathcal{S}} Q^{k+1}, \rho_3 \Delta\tau^{k+1} + \nabla_{\Delta\tau} Q^{k+1}) \quad (29) \\ &\in \partial F(\mathcal{X}^{k+1}, \mathcal{Y}^{k+1}, \mathcal{S}^{k+1}, \Delta\tau^{k+1}). \end{aligned}$$

Hence, we deduce

$$\text{dist}(0, \partial F(\mathcal{Z}^{k+1})) \leq \|w^{k+1}\|_F. \quad (30)$$

It follows from Theorem 1 that the sequence  $\{\mathcal{Z}^k\}$  is bounded. Therefore, there exists a compact set  $\mathfrak{D}$  such that  $\mathcal{Z}^k \subset \mathfrak{D}$  for

any  $k$ . Note that  $Q$  in (6) is a quadratic function, then  $\nabla Q$  is Lipschitz continuous on any bounded subset of  $\mathfrak{D}$  with a Lipschitz constant  $L$ . Hence, we obtain that

$$\begin{aligned} & \|\nabla_{\mathcal{X}} Q(\mathcal{X}^{k+1}, \mathcal{Y}^{k+1}, \mathcal{S}^{k+1}, \Delta\tau^{k+1}) + \rho_1 \mathcal{X}^{k+1}\|_F \\ & \leq \|\nabla_{\mathcal{X}} Q(\mathcal{X}^{k+1}, \mathcal{Y}^k, \mathcal{S}^k, \Delta\tau^k) + \rho_1 \mathcal{X}^{k+1}\|_F \\ & \quad + \|\nabla_{\mathcal{X}} Q(\mathcal{X}^{k+1}, \mathcal{Y}^{k+1}, \mathcal{S}^{k+1}, \Delta\tau^{k+1}) \\ & \quad - \nabla_{\mathcal{X}} Q(\mathcal{X}^{k+1}, \mathcal{Y}^k, \mathcal{S}^k, \Delta\tau^k)\|_F \\ & \leq \bar{d} \|\mathcal{X}^{k+1} - \mathcal{X}^k\|_F + \|\nabla_{\mathcal{X}} Q(\mathcal{X}^{k+1}, \mathcal{Y}^{k+1}, \mathcal{S}^{k+1}, \Delta\tau^{k+1}) \\ & \quad - \nabla_{\mathcal{X}} Q(\mathcal{X}^{k+1}, \mathcal{Y}^k, \mathcal{S}^k, \Delta\tau^k)\|_F \\ & \leq \bar{d} \|\mathcal{X}^{k+1} - \mathcal{X}^k\|_F + L \|\mathcal{Y}^{k+1}, \mathcal{S}^{k+1}, \Delta\tau^{k+1}\|_F \\ & \leq \bar{d} \|\mathcal{X}^{k+1} - \mathcal{X}^k\|_F + L \|\mathcal{Z}^{k+1} - \mathcal{Z}^k\|_F \\ & \leq (\bar{d} + L) \|\mathcal{Z}^{k+1} - \mathcal{Z}^k\|_F, \end{aligned} \quad (31)$$

where the second inequality holds by (26). In a similar vein, one can get

$$\begin{aligned} & \|\nabla_{\mathcal{Y}} Q(\mathcal{X}^{k+1}, \mathcal{Y}^{k+1}, \mathcal{S}^{k+1}, \Delta\tau^{k+1}) + \rho_2 \mathcal{Y}^{k+1}\|_F \\ & \leq (\bar{d} + L) \|\mathcal{Z}^{k+1} - \mathcal{Z}^k\|_F, \\ & \|\nabla_{\mathcal{S}} Q(\mathcal{X}^{k+1}, \mathcal{Y}^{k+1}, \mathcal{S}^{k+1}, \Delta\tau^{k+1}) + \mathcal{S}_1^{k+1}\|_F \\ & \leq (\bar{d} + L) \|\mathcal{Z}^{k+1} - \mathcal{Z}^k\|_F, \\ & \|\nabla_{\Delta\tau} Q(\mathcal{X}^{k+1}, \mathcal{Y}^{k+1}, \mathcal{S}^{k+1}, \Delta\tau^{k+1}) + \rho_3 \Delta\tau^{k+1}\|_F \\ & \leq \bar{d} \|\mathcal{Z}^{k+1} - \mathcal{Z}^k\|_F. \end{aligned} \quad (32)$$

Combining (29), (30), (31) and (32), we get that

$$\text{dist}(0, \partial F(\mathcal{Z}^{k+1})) \leq \|w^{k+1}\|_F \leq C \|\mathcal{Z}^{k+1} - \mathcal{Z}^k\|_F, \quad (33)$$

where  $C = 4\bar{d} + 3L$ .

(ii) Define  $h(s) := \frac{\mu}{1-\theta}(s - F(\mathcal{Z}^*))^{1-\theta}$ , where  $\mu > 0$  is a constant and  $\theta \in (0, 1)$ . Observe that  $h(s)$  is a concave function for  $s \geq F(\mathcal{Z}^*)$ , and its derivative function is  $h'(s) = \frac{\mu}{(s-F(\mathcal{Z}^*))^\theta}$  for  $s > F(\mathcal{Z}^*)$ . It then follows from the concavity of the function  $h(s)$  that

$$\begin{aligned} h(F(\mathcal{Z}^k)) - h(F(\mathcal{Z}^{k+1})) &\geq h'(F(\mathcal{Z}^k))(F(\mathcal{Z}^k) - F(\mathcal{Z}^{k+1})) \\ &= \frac{\mu}{(F(\mathcal{Z}^k) - F(\mathcal{Z}^*))^\theta} (F(\mathcal{Z}^k) - F(\mathcal{Z}^{k+1})). \end{aligned} \quad (34)$$

Note that  $F$  in (5) is a proper closed semi-algebraic function when  $p$  is rational, whose proof is given in Theorem 1. Therefore, we know that  $F$  satisfies the KL property at  $\mathcal{Z}^*$  with  $\varphi(s) = \mu s^{1-\theta}$  [51], where  $\varphi$  comes from Definition 9, and  $\theta \in [0, 1)$ ,  $\mu > 0$ . Notice that the KL inequality in (20) yields

$$\begin{aligned} (F(\mathcal{Z}^k) - F(\mathcal{Z}^*))^\theta &\leq \mu(1-\theta) \text{dist}(0, \partial F(\mathcal{Z}^k)) \\ &\leq \mu C \|\mathcal{Z}^k - \mathcal{Z}^{k-1}\|_F, \end{aligned} \quad (35)$$

where the last inequality holds by (33) and  $\theta \in [0, 1)$ .

On the other hand, it follows from (22) that

$$\begin{aligned} & F(\mathcal{Z}^k) - F(\mathcal{Z}^{k+1}) \\ & \geq \frac{\alpha^k}{2} \|\mathcal{X}^{k+1} - \mathcal{X}^k\|_F^2 + \frac{\beta^k}{2} \|\mathcal{Y}^{k+1} - \mathcal{Y}^k\|_F^2 \\ & \quad + \frac{\gamma^k}{2} \|\mathcal{S}^{k+1} - \mathcal{S}^k\|_F^2 + \frac{\xi^k}{2} \|\Delta\tau^{k+1} - \Delta\tau^k\|_F^2 \\ & \geq \frac{\delta^k}{2} \|\mathcal{Z}^{k+1} - \mathcal{Z}^k\|_F^2, \end{aligned} \quad (36)$$

where  $\delta^k := \min\{\alpha^k, \beta^k, \gamma^k, \xi^k\} \geq \underline{d}$ . In light of (34), (35), and (36), we have

$$h(F(\mathcal{Z}^k)) - h(F(\mathcal{Z}^{k+1})) \geq \frac{\delta^k \|\mathcal{Z}^{k+1} - \mathcal{Z}^k\|_F^2}{2C \|\mathcal{Z}^k - \mathcal{Z}^{k-1}\|_F},$$

which implies that

$$\begin{aligned} & 2\|\mathcal{Z}^{k+1} - \mathcal{Z}^k\|_F \\ & \leq 2\left(\frac{2C}{\delta^k}\right)^{\frac{1}{2}} \left(h(F(\mathcal{Z}^k)) - h(F(\mathcal{Z}^{k+1}))\right)^{\frac{1}{2}} \|\mathcal{Z}^k - \mathcal{Z}^{k-1}\|_F^{\frac{1}{2}} \\ & \leq \frac{2C}{\delta^k} \left(h(F(\mathcal{Z}^k)) - h(F(\mathcal{Z}^{k+1}))\right) + \|\mathcal{Z}^k - \mathcal{Z}^{k-1}\|_F, \end{aligned}$$

where the second inequality holds by the fact that  $a^2 + b^2 \geq 2ab$ . Summing the above inequality from  $k$  to infinity to obtain

$$\begin{aligned} & \sum_{j=k}^{\infty} \frac{2C}{\delta^k} \left(h(F(\mathcal{Z}^j)) - h(F(\mathcal{Z}^{j+1}))\right) + \sum_{j=k}^{\infty} \|\mathcal{Z}^j - \mathcal{Z}^{j-1}\|_F \\ & \geq 2 \sum_{j=k}^{\infty} \|\mathcal{Z}^{j+1} - \mathcal{Z}^j\|_F. \end{aligned}$$

Therefore, we deduce that

$$\begin{aligned} & \sum_{j=k}^{\infty} \|\mathcal{Z}^{j+1} - \mathcal{Z}^j\|_F \\ & \leq \|\mathcal{Z}^k - \mathcal{Z}^{k-1}\|_F + \frac{2C}{\delta^k} \sum_{j=k}^{\infty} \left(h(F(\mathcal{Z}^j)) - h(F(\mathcal{Z}^{j+1}))\right) \\ & = \|\mathcal{Z}^k - \mathcal{Z}^{k-1}\|_F + \frac{2C}{\delta^k} \left(h(F(\mathcal{Z}^k)) - \lim_{j \rightarrow \infty} h(F(\mathcal{Z}^j))\right) \\ & \leq \|\mathcal{Z}^k - \mathcal{Z}^{k-1}\|_F + \frac{2C}{\delta^k} h(F(\mathcal{Z}^k)) \\ & = \|\mathcal{Z}^k - \mathcal{Z}^{k-1}\|_F + \frac{2C\mu}{\delta^k(1-\theta)} (F(\mathcal{Z}^k) - F(\mathcal{Z}^*))^{1-\theta} \\ & \leq \|\mathcal{Z}^k - \mathcal{Z}^{k-1}\|_F + \frac{\mu}{\rho(1-\theta)} (F(\mathcal{Z}^k) - F(\mathcal{Z}^*))^{1-\theta}, \end{aligned}$$

where  $\rho := \frac{\underline{d}}{2C}$ .

(iii) Setting  $k = 1$  in (27) yields

$$\begin{aligned} & \sum_{j=0}^{\infty} \|\mathcal{Z}^{j+1} - \mathcal{Z}^j\|_F = \sum_{j=1}^{\infty} \|\mathcal{Z}^{j+1} - \mathcal{Z}^j\|_F + \|\mathcal{Z}^1 - \mathcal{Z}^0\|_F \\ & \leq 2\|\mathcal{Z}^1 - \mathcal{Z}^0\|_F + \frac{\mu}{\rho(1-\theta)} (F(\mathcal{Z}^1) - F(\mathcal{Z}^*))^{1-\theta} < +\infty, \end{aligned} \quad (37)$$

where  $\mathcal{Z}^*$  is a critical point of  $F$ .

(iv) Define  $g_k(\mathcal{Z}) := \mathcal{Z}^{k+1} - \mathcal{Z}^k$ . From Theorem 1, we obtain that  $\{\mathcal{Z}^{k+1}\}$  is bounded. Denote  $E$  to be a bounded measurable set and  $\{\mathcal{Z}^{k+1}\} \subset E$ . Thus  $g_k(\mathcal{Z})$  is a measurable

function on  $E$ . In addition,  $\|g_k(\mathcal{Z})\|_F = \|\mathcal{Z}^{k+1} - \mathcal{Z}^k\|_F < \infty$  for any  $k = 1, 2, \dots$ . Note that, for any positive integer  $n$ , we get that  $\sum_{k=1}^n g_k(\mathcal{Z}) = \sum_{k=1}^n (\mathcal{Z}^{k+1} - \mathcal{Z}^k) = \mathcal{Z}^{n+1} - \mathcal{Z}^1$ . Therefore,  $\sum_{k=1}^n g_k(\mathcal{Z})$  converges to  $\mathcal{Z}^* - \mathcal{Z}^1$  as  $n$  tends to infinity, which follows from the fact that the sequence  $\{\mathcal{Z}^k\}$  converges to  $\mathcal{Z}^*$ . Combining [57, Corollary 6.4] with  $\mathcal{Z}^k \rightarrow \mathcal{Z}^*, k \rightarrow \infty$ , we get

$$\begin{aligned} \sum_{j=k}^{\infty} \|\mathcal{Z}^{j+1} - \mathcal{Z}^j\|_F & \geq \left\| \sum_{j=k}^{\infty} (\mathcal{Z}^{j+1} - \mathcal{Z}^j) \right\|_F \\ & = \left\| \lim_{n \rightarrow \infty} \sum_{j=k}^n (\mathcal{Z}^{j+1} - \mathcal{Z}^j) \right\|_F \\ & = \left\| \lim_{n \rightarrow \infty} \mathcal{Z}^{n+1} - \mathcal{Z}^k \right\|_F = \|\mathcal{Z}^k - \mathcal{Z}^*\|_F. \end{aligned}$$

The proof is completed.  $\blacksquare$

*Proof of Theorem 2:* (i) When  $\theta = 0$ , we must have  $F(\mathcal{Z}^{k_0}) = F(\mathcal{Z}^*)$  for some  $k_0$ . Otherwise, for sufficiently large  $k$ , we have  $F(\mathcal{Z}^k) > F(\mathcal{Z}^*)$ . It follows from (35) that  $\mu \text{dist}(0, \partial F(\mathcal{Z}^k)) \geq 1$  for all  $k$ , which is impossible since  $\mathcal{Z}^k \rightarrow \mathcal{Z}^*$  and  $0 \in \partial F(\mathcal{Z}^*)$ . Therefore, there exists some  $k_0$  such that  $F(\mathcal{Z}^{k_0}) = F(\mathcal{Z}^*)$ . Since  $F$  is monotonically non-increasing, we have that  $\mathcal{Z}^k = \mathcal{Z}^{k_0} = \mathcal{Z}^*$  for all  $k > k_0$ .

(ii) Let  $\Delta_k := \sum_{j=k}^{\infty} \|\mathcal{Z}^{j+1} - \mathcal{Z}^j\|_F$ . It follows from Lemma 1(iv) that  $\Delta_k \geq \|\mathcal{Z}^k - \mathcal{Z}^*\|_F$ . Moreover, Lemma 1(ii) leads to

$$\begin{aligned} \Delta_k & = \sum_{j=k}^{\infty} \|\mathcal{Z}^{j+1} - \mathcal{Z}^j\|_F \\ & \leq \|\mathcal{Z}^k - \mathcal{Z}^{k-1}\|_F + \frac{\mu}{\rho(1-\theta)} (F(\mathcal{Z}^k) - F(\mathcal{Z}^*))^{1-\theta} \\ & = \|\mathcal{Z}^k - \mathcal{Z}^{k-1}\|_F + \frac{\mu}{\rho(1-\theta)} ((F(\mathcal{Z}^k) - F(\mathcal{Z}^*))^{\theta})^{\frac{1-\theta}{\theta}} \\ & \leq \|\mathcal{Z}^k - \mathcal{Z}^{k-1}\|_F + \frac{\mu}{\rho(1-\theta)} \left(\mu C \|\mathcal{Z}^k - \mathcal{Z}^{k-1}\|_F\right)^{\frac{1-\theta}{\theta}} \\ & = (\Delta_{k-1} - \Delta_k) + c_1 (\Delta_{k-1} - \Delta_k)^{\frac{1-\theta}{\theta}}, \end{aligned} \quad (38)$$

where the second inequality holds by (35) and the last equality holds by letting  $c_1 := \frac{\mu}{\rho(1-\theta)} (\mu C)^{\frac{1-\theta}{\theta}}$ .

Let  $S_k := \sum_{j=0}^k \|\mathcal{Z}^{j+1} - \mathcal{Z}^j\|_F$ . By Lemma 1(iii), we know that  $\sum_{j=0}^{\infty} \|\mathcal{Z}^{j+1} - \mathcal{Z}^j\|_F < +\infty$ , which implies that  $\lim_{k \rightarrow \infty} S_k = \sum_{j=0}^{\infty} \|\mathcal{Z}^{j+1} - \mathcal{Z}^j\|_F$  exists. Note that  $\Delta_k = \sum_{j=k}^{\infty} \|\mathcal{Z}^{j+1} - \mathcal{Z}^j\|_F = \sum_{j=0}^{\infty} \|\mathcal{Z}^{j+1} - \mathcal{Z}^j\|_F - S_{k-1}$ . Hence

$$\lim_{k \rightarrow \infty} \Delta_k = \sum_{j=0}^{\infty} \|\mathcal{Z}^{j+1} - \mathcal{Z}^j\|_F - \lim_{k \rightarrow \infty} S_{k-1} = 0. \quad (39)$$

If  $\theta \in (0, \frac{1}{2}]$ , then  $\frac{1-\theta}{\theta} \geq 1$ . Notice that  $\Delta_k$  is monotonically non-increasing. We observe that (38) reads (for  $k$  sufficiently large)  $\Delta_k \leq c_2(\Delta_{k-1} - \Delta_k)$ , where  $c_2 = 1 + c_1 > 0$ . Consequently, we have  $\Delta_k \leq \frac{c_2}{c_2+1} \Delta_{k-1}$ . Let  $\vartheta := \frac{c_2}{c_2+1} \in (0, 1)$  and  $c = \Delta_0$ . By Lemma 1(iv), we get that

$$\|\mathcal{Z}^k - \mathcal{Z}^*\|_F \leq \Delta_k \leq \vartheta \Delta_{k-1} \leq \dots \leq \vartheta^k \Delta_0 = c\vartheta^k.$$

(iii) If  $\theta \in (\frac{1}{2}, 1)$ , then  $0 < \frac{1-\theta}{\theta} < 1$ . Therefore, by (38), we get that there exists a positive integer  $K_0$  such that for any  $k > K_0$ ,

$$\Delta_k^{\frac{\theta}{1-\theta}} \leq c_3(\Delta_{k-1} - \Delta_k), \quad (40)$$

where  $c_3 = (1 + c_1)^{\frac{\theta}{1-\theta}}$ .

Define  $f(s) := s^{-\frac{\theta}{1-\theta}}$ ,  $s > 0$ . Let  $R \in (1, \infty)$ . First, assume that  $f(\Delta_k) \leq Rf(\Delta_{k-1})$ , we can obtain that

$$\begin{aligned} c_3^{-1} &\leq \Delta_k^{-\frac{\theta}{1-\theta}}(\Delta_{k-1} - \Delta_k) = f(\Delta_k)(\Delta_{k-1} - \Delta_k) \\ &\leq \int_{\Delta_k}^{\Delta_{k-1}} Rf(\Delta_{k-1})ds \leq \int_{\Delta_k}^{\Delta_{k-1}} Rf(s)ds \\ &= \frac{R(1-\theta)}{1-2\theta} \left( \Delta_{k-1}^{\frac{1-2\theta}{1-\theta}} - \Delta_k^{\frac{1-2\theta}{1-\theta}} \right), \end{aligned} \quad (41)$$

where the first inequality holds by (40). Let  $v := \frac{1-2\theta}{1-\theta} < 0$  and  $e_1 := c_3^{-1} \frac{2\theta-1}{R(1-\theta)}$ . The (41) implies that

$$\Delta_k^v - \Delta_{k-1}^v \geq e_1 > 0. \quad (42)$$

Second, assume that  $f(\Delta_k) > Rf(\Delta_{k-1})$ , i.e.,  $\Delta_k^{-\frac{\theta}{1-\theta}} > R\Delta_{k-1}^{-\frac{\theta}{1-\theta}}$ , which implies that  $\Delta_k < R^{-\frac{1-\theta}{\theta}}\Delta_{k-1}$ . It follows from  $v = \frac{1-2\theta}{1-\theta} < 0$  that

$$\Delta_k^v > (R^{-\frac{1-\theta}{\theta}})^v \Delta_{k-1}^v,$$

which implies  $\Delta_k^v - \Delta_{k-1}^v \geq ((R^{-\frac{1-\theta}{\theta}})^v - 1)\Delta_{k-1}^v$ . Since  $R^{-\frac{1-\theta}{\theta}} \in (0, 1)$ , we have  $(R^{-\frac{1-\theta}{\theta}})^v - 1 > 0$ . Moreover, it can be derived from (39) that there exist a constant  $c_4 > 0$  and a positive integer  $K_1$  such that  $\Delta_{k-1} \leq c_4$  for any  $k > K_1$ . Therefore, we have  $((R^{-\frac{1-\theta}{\theta}})^v - 1)\Delta_{k-1}^v > ((R^{-\frac{1-\theta}{\theta}})^v - 1)c_4^v$ . Let  $e_2 = ((R^{-\frac{1-\theta}{\theta}})^v - 1)c_4^v$ , we can deduce that

$$\Delta_k^v - \Delta_{k-1}^v > e_2 > 0. \quad (43)$$

Let  $\hat{e} := \min\{e_1, e_2\}$ . Combining (42) with (43), we obtain

$$\Delta_k^v - \Delta_{k-1}^v \geq \hat{e}. \quad (44)$$

Let  $\hat{k} := \max\{K_0, K_1\}$ . As a consequence, for any  $k \geq 2\hat{k}$ , we have  $\Delta_k^v - \Delta_{\hat{k}}^v = \sum_{l=\hat{k}+1}^k (\Delta_l^v - \Delta_{l-1}^v) \geq \hat{e}(k - \hat{k})$ , which yields

$$\Delta_k^v \geq \Delta_{\hat{k}}^v + \hat{e}(k - \hat{k}) \geq \hat{e}(k - \hat{k}) \geq \frac{\hat{e}k}{2}, \quad (45)$$

where the last inequality holds by  $\hat{k} \leq \frac{k}{2}$ . Let  $c := (\frac{\hat{e}}{2})^{\frac{1}{v}}$ . Therefore, we deduce that  $\|\mathcal{Z}^k - \mathcal{Z}^*\|_F \leq \Delta_k \leq ck^{\frac{1}{v}} = ck^{-\frac{1-\theta}{2\theta-1}}$ , where the first inequality holds by Lemma 1(iv). This completes the proof.  $\blacksquare$

## REFERENCES

- [1] R. Szeliski, "Image alignment and stitching: A tutorial," *Foundations and Trends® in Computer Graphics and Vision*, vol. 2, no. 1, pp. 1–104, 2007.
- [2] Y. Peng, A. Ganesh, J. Wright, W. Xu, and Y. Ma, "RASL: Robust alignment by sparse and low-rank decomposition for linearly correlated images," *IEEE Trans. Pattern Anal. Mach. Intell.*, vol. 34, no. 11, pp. 2233–2246, Nov. 2012.
- [3] A. Yilmaz, O. Javed, and M. Shah, "Object tracking: A survey," *ACM Comput. Sur.*, vol. 38, no. 4, p. 13, 2006.
- [4] J. Wright, A. Y. Yang, A. Ganesh, S. S. Sastry, and Y. Ma, "Robust face recognition via sparse representation," *IEEE Trans. Pattern Anal. Mach. Intell.*, vol. 31, no. 2, pp. 210–227, Feb. 2009.
- [5] Y. Wu, B. Shen, and H. Ling, "Online robust image alignment via iterative convex optimization," in *2012 IEEE Conf. Computer Vision Pattern Recognit.* IEEE, 2012, pp. 1808–1814.
- [6] E. G. Learned-Miller, "Data driven image models through continuous joint alignment," *IEEE Trans. Pattern Anal. Mach. Intell.*, vol. 28, no. 2, pp. 236–250, Feb. 2006.
- [7] M. Cox, S. Sridharan, S. Lucey, and J. Cohn, "Least squares congealing for unsupervised alignment of images," in *2008 IEEE Conf. Computer Vision Pattern Recognit.* IEEE, 2008, pp. 1–8.
- [8] —, "Least-squares congealing for large numbers of images," in *2009 IEEE 12th Inter. Conf. Computer Vision.* IEEE, 2009, pp. 1949–1956.
- [9] A. Vedaldi, G. Guidi, and S. Soatto, "Joint data alignment up to (lossy) transformations," in *2008 IEEE Conf. Computer Vision Pattern Recognit.* IEEE, 2008, pp. 1–8.
- [10] Y. Ma, S. Soatto, J. Košecká, and S. Sastry, *An Invitation to 3-D Vision: From Images to Geometric Models*. New York: Springer, 2004, vol. 26.
- [11] J. He, D. Zhang, L. Balzano, and T. Tao, "Iterative Grassmannian optimization for robust image alignment," *Image Vis. Comput.*, vol. 32, no. 10, pp. 800–813, 2014.
- [12] J. Fan and R. Li, "Variable selection via nonconcave penalized likelihood and its oracle properties," *J. Am. Stat. Assoc.*, vol. 96, no. 456, pp. 1348–1360, 2001.
- [13] H. Zou, "The adaptive lasso and its oracle properties," *J. Am. Stat. Assoc.*, vol. 101, no. 476, pp. 1418–1429, 2006.
- [14] C.-H. Zhang, "Nearly unbiased variable selection under minimax concave penalty," *Ann. Stat.*, vol. 38, no. 2, pp. 894–942, 2010.
- [15] X. Chen, Z. Han, Y. Wang, Y. Tang, and H. Yu, "Nonconvex plus quadratic penalized low-rank and sparse decomposition for noisy image alignment," *Sci. China Inform. Sci.*, vol. 59, no. 5, p. 052107, 2016.
- [16] W. Song, J. Zhu, Y. Li, and C. Chen, "Image alignment by online robust PCA via stochastic gradient descent," *IEEE Trans. Circuits Syst. Video Technol.*, vol. 26, no. 7, pp. 1241–1250, Jul. 2016.
- [17] Q. Zheng, Y. Wang, and P. A. Heng, "Online subspace learning from gradient orientations for robust image alignment," *IEEE Trans. Image Process.*, vol. 28, no. 7, pp. 3383–3394, Jul. 2019.
- [18] X. Zhang, D. Wang, Z. Zhou, and Y. Ma, "Simultaneous rectification and alignment via robust recovery of low-rank tensors," *In Adv. Neural Inform. Process. Syst.*, vol. 2, pp. 1637–1645, 2013.
- [19] J. Liu, P. Musialski, P. Wonka, and J. Ye, "Tensor completion for estimating missing values in visual data," *IEEE Trans. Pattern Anal. Mach. Intell.*, vol. 35, no. 1, pp. 208–220, Jan. 2013.
- [20] P. Li, J. Feng, X. Jin, L. Zhang, X. Xu, and S. Yan, "Online robust low-rank tensor modeling for streaming data analysis," *IEEE Trans. Neural Netw. Learn. Syst.*, vol. 30, no. 4, pp. 1061–1075, Apr. 2019.
- [21] F. Bunea, Y. She, and M. H. Wegkamp, "Optimal selection of reduced rank estimators of high-dimensional matrices," *Ann. Stat.*, vol. 39, no. 2, pp. 1282–1309, 2011.
- [22] X. Zhang, D. Wang, Z. Zhou, and Y. Ma, "Robust low-rank tensor recovery with rectification and alignment," *IEEE Trans. Pattern Anal. Mach. Intell.*, vol. 43, no. 1, pp. 238–255, Jan. 2021.
- [23] B. Romera-Paredes and M. Pontil, "A new convex relaxation for tensor completion," *Advances in Neural Information Processing Systems*, pp. 2967–2975, 2013.
- [24] C. Mu, B. Huang, J. Wright, and D. Goldfarb, "Square deal: Lower bounds and improved relaxations for tensor recovery," in *Inter. Conf. Machine Learn.* PMLR, 2014, pp. 73–81.
- [25] M. E. Kilmer and C. D. Martin, "Factorization strategies for third-order tensors," *Linear Algebra Appl.*, vol. 435, no. 3, pp. 641–658, 2011.
- [26] M. E. Kilmer, K. Braman, N. Hao, and R. C. Hoover, "Third-order tensors as operators on matrices: A theoretical and computational framework with applications in imaging," *SIAM J. Matrix Anal. Appl.*, vol. 34, no. 1, pp. 148–172, 2013.
- [27] O. Semerci, N. Hao, M. E. Kilmer, and E. L. Miller, "Tensor-based formulation and nuclear norm regularization for multienergy computed tomography," *IEEE Trans. Image Process.*, vol. 23, no. 4, pp. 1678–1693, Apr. 2014.
- [28] Z. Zhang, G. Ely, S. Aeron, N. Hao, and M. Kilmer, "Novel methods for multilinear data completion and de-noising based on tensor-SVD," in *2014 IEEE Conf. Computer Vision Pattern Recognition.* IEEE, 2014, pp. 3842–3849.
- [29] C. Lu, J. Feng, Y. Chen, W. Liu, Z. Lin, and S. Yan, "Tensor robust principal component analysis with a new tensor nuclear norm," *IEEE Trans. Pattern Anal. Mach. Intell.*, vol. 42, no. 4, pp. 925–938, Apr. 2020.

[30] X. Zhang and M. K. Ng, "A corrected tensor nuclear norm minimization method for noisy low-rank tensor completion," *SIAM J. Imaging Sci.*, vol. 12, no. 2, pp. 1231–1273, 2019.

[31] Y.-B. Zheng, T.-Z. Huang, X.-L. Zhao, T.-X. Jiang, T.-H. Ma, and T.-Y. Ji, "Mixed noise removal in hyperspectral image via low-fibered-rank regularization," *IEEE Trans. Geosci. Remote Sens.*, vol. 58, no. 1, pp. 734–749, Jan. 2020.

[32] N. Hao, M. E. Kilmer, K. Braman, and R. C. Hoover, "Facial recognition using tensor-tensor decompositions," *SIAM J. Imaging Sci.*, vol. 6, no. 1, pp. 437–463, 2013.

[33] P. Zhou, C. Lu, Z. Lin, and C. Zhang, "Tensor factorization for low-rank tensor completion," *IEEE Trans. Image Process.*, vol. 27, no. 3, pp. 1152–1163, Mar. 2018.

[34] C. D. Martin, R. Shafer, and B. LaRue, "An order- $p$  tensor factorization with applications in imaging," *SIAM J. Sci. Comput.*, vol. 35, no. 1, pp. A474–A490, 2013.

[35] J. Hou, F. Zhang, H. Qiu, J. Wang, Y. Wang, and D. Meng, "Robust low-tubal-rank tensor recovery from binary measurements," *IEEE Trans. Pattern Anal. Machine Intell.*, vol. 44, no. 8, pp. 4355–4373, Aug. 2022.

[36] J.-L. Wang, T.-Z. Huang, X.-L. Zhao, T.-X. Jiang, and M. K. Ng, "Multi-dimensional visual data completion via low-rank tensor representation under coupled transform," *IEEE Trans. Image Process.*, vol. 30, pp. 3581–3596, Mar. 2021.

[37] D. Qiu, M. Bai, M. K. Ng, and X. Zhang, "Nonlocal robust tensor recovery with nonconvex regularization," *Inverse Problems*, vol. 37, no. 3, p. 035001, 2021.

[38] G. Song, M. K. Ng, and X. Zhang, "Robust tensor completion using transformed tensor singular value decomposition," *Numer. Linear Algebra Appl.*, vol. 27, no. 3, p. e2299, 2020.

[39] X. Zhang and M. K.-P. Ng, "Low rank tensor completion with Poisson observations," *IEEE Trans. Pattern Anal. Mach. Intell.*, vol. 44, no. 8, pp. 4239–4251, Aug. 2022.

[40] G.-J. Song, M. K. Ng, and X. Zhang, "Tensor completion by multi-rank via unitary transformation," *arXiv:2012.08784*, 2020.

[41] M. K. Ng, X. Zhang, and X.-L. Zhao, "Patched-tube unitary transform for robust tensor completion," *Pattern Recognit.*, vol. 100, p. 107181, 2020.

[42] D. Qiu, M. Bai, M. K. Ng, and X. Zhang, "Robust low transformed multi-rank tensor methods for image alignment," *J. Sci. Comput.*, vol. 87, no. 1, p. 24, 2021.

[43] K. Jittorntrum and M. R. Osborne, "Strong uniqueness and second order convergence in nonlinear discrete approximation," *Numer. Math.*, vol. 34, no. 4, pp. 439–455, 1980.

[44] J. Bolte, S. Sabach, and M. Teboulle, "Proximal alternating linearized minimization for nonconvex and nonsmooth problems," *Math. Program.*, vol. 146, no. 1-2, pp. 459–494, 2014.

[45] T. G. Kolda and B. W. Bader, "Tensor decompositions and applications," *SIAM Rev.*, vol. 51, no. 3, pp. 455–500, 2009.

[46] E. Kernfeld, M. Kilmer, and S. Aeron, "Tensor–tensor products with invertible linear transforms," *Linear Algebra Appl.*, vol. 485, pp. 545–570, 2015.

[47] G. Marjanovic and V. Solo, "On  $\ell_q$  optimization and matrix completion," *IEEE Trans. Signal Process.*, vol. 60, no. 11, pp. 5714–5724, Nov. 2012.

[48] H. Attouch, J. Bolte, and B. F. Svaiter, "Convergence of descent methods for semi-algebraic and tame problems: proximal algorithms, forward–backward splitting, and regularized Gauss–Seidel methods," *Math. Program.*, vol. 137, no. 1-2, pp. 91–129, 2013.

[49] H. Attouch and J. Bolte, "On the convergence of the proximal algorithm for nonsmooth functions involving analytic features," *Math. Program.*, vol. 116, no. 1, pp. 5–16, 2009.

[50] G. Li and T. K. Pong, "Calculus of the exponent of Kurdyka–Łojasiewicz inequality and its applications to linear convergence of first-order methods," *Found. Comput. Math.*, vol. 18, no. 5, pp. 1199–1232, 2017.

[51] H. Attouch, J. Bolte, P. Redont, and A. Soubeyran, "Proximal alternating minimization and projection methods for nonconvex problems: An approach based on the Kurdyka–Łojasiewicz inequality," *Math. Oper. Res.*, vol. 35, no. 2, pp. 438–457, 2010.

[52] P. Yu, G. Li, and T. K. Pong, "Kurdyka–Łojasiewicz exponent via inf-projection," *Found. Comput. Math.*, vol. 22, no. 4, pp. 1171–1217, 2022.

[53] Y. Xu, R. Hao, W. Yin, and Z. Su, "Parallel matrix factorization for low-rank tensor completion," *Inverse Probl. Imaging*, vol. 9, no. 2, pp. 601–624, 2015.

[54] Z. Wen, W. Yin, and Y. Zhang, "Solving a low-rank factorization model for matrix completion by a nonlinear successive over-relaxation algorithm," *Math. Program. Comput.*, vol. 4, no. 4, pp. 333–361, 2012.

[55] X. Zhang and M. K. Ng, "Sparse nonnegative tensor factorization and completion with noisy observations," *IEEE Trans. Inf. Theory*, vol. 68, no. 4, pp. 2551–2572, Apr. 2022.

[56] R. T. Rockafellar and R. J.-B. Wets, *Variational Analysis*. 3rd ed., Berlin: Springer, 2009.

[57] M. Zhou, *Real Analysis (In Chinese)*. Beijing: Peking University Press, 1995.